REPORT DOCUMENTATION PAGE

Form Approved
OMB No. 0704-0188

1. REPORT DATE *(DD-MM-YYYY)*	2. REPORT TYPE	3. DATES COVERED *(From - To)*
03-12-2008	Final	01 Dec 2004 to 31 Dec 2006

4. TITLE AND SUBTITLE

Experiments on the Receptivity of Transient Disturbances to Surface Roughness and Freestream Turbulence

5a. CONTRACT NUMBER

5b. GRANT NUMBER
FA9550-05-1-0048

5c. PROGRAM ELEMENT NUMBER

6. AUTHOR(S)
Edward B. White

5d. PROJECT NUMBER

5e. TASK NUMBER

5f. WORK UNIT NUMBER

7. PERFORMING ORGANIZATION NAME(S) AND ADDRESS(ES)
Case Western Reserve University
10900 Euclid Ave.
Cleveland, OH 44106

8. PERFORMING ORGANIZATION REPORT NUMBER

9. SPONSORING/MONITORING AGENCY NAME(S) AND ADDRESS(ES)
Air Force Office of Scientific Research
875 North Randolph Street
Arlington, Va., 22203
Dr Rhett Jeffries/NA

10. SPONSOR/MONITOR'S ACRONYM(S)

11. SPONSOR/MONITOR'S REPORT NUMBER(S)

12. DISTRIBUTION/AVAILABILITY STATEMENT

Approved for public release,
distribution unlimited

AFRL-SR-AR-TR-08-0045

13. SUPPLEMENTARY NOTES

14. ABSTRACT

Transient growth is a boundary-layer instability mechanism that leads to algebraic growth of disturbances generated by surface roughness and freestream turbulence. An earlier research program verified that stationary, roughness-induced disturbances undergo transient growth but that these disturbances are sub-optimal and depend critically on the details of the receptivity process. This project seeks to provide a more complete understanding of the receptivity of transient disturbances to regular and random surface roughness as well as freestream turbulence. This objective is pursued through three separate tracks. First, a technique is developed to permit a rigorous decomposition of measured steady disturbances across the continuous spectrum of Orr–Sommerfeld/Squire eigenmodes. Second, the receptivity and transient growth of steady disturbances generated by quasi-random distributed surface roughness is investigated. Third, transient disturbances generated by controlled freestream turbulence are to be investigated.

15. SUBJECT TERMS

transient growth, boundary-layer instability, boundary-layer transition, laminar-turbulent transition, roughness

16. SECURITY CLASSIFICATION OF:			17. LIMITATION OF ABSTRACT	18. NUMBER OF PAGES	19a. NAME OF RESPONSIBLE PERSON
a. REPORT	b. ABSTRACT	c. THIS PAGE			
				50	19b. TELEPHONE NUMBER *(Include area code)*

Standard Form 298 (Rev. 8/98)
Prescribed by ANSI Std. Z39.18

Final Report for AFOSR Grant FA9550-05-1-0048

Experiments on the Receptivity of Transient Disturbances to Surface Roughness and Freestream Turbulence

Edward B. White[1]

Department of Mechanical and Aerospace Engineering
Case Western Reserve University
10900 Euclid Ave.
Cleveland, OH 44106-7222

Summary

Transient growth is a boundary-layer instability mechanism that leads to algebraic growth of disturbances generated by surface roughness and freestream turbulence. An earlier research program (AFOSR FA9620-02-1-0058, 12/01–11/04) verified that stationary, roughness-induced disturbances undergo transient growth but that these disturbances are sub-optimal and depend critically on the details of the receptivity process. This project seeks to provide a more complete understanding of the receptivity of transient disturbances to regular and random surface roughness as well as freestream turbulence. This objective is pursued through three separate tracks. First, a technique is developed to permit a rigorous decomposition of measured steady disturbances across the continuous spectrum of Orr–Sommerfeld/Squire (OSS) eigenmodes. Second, the receptivity and transient growth of steady disturbances generated by quasi-random distributed surface roughness is investigated. Third, transient disturbances generated by controlled freestream turbulence are to be investigated.

This work was originally proposed as a 36-month project to be conducted at Case Western Reserve University. However, the PI, Prof. Edward White, accepted a new position at Texas A&M University (TAMU) starting January, 2007, the project's 25th month. At that time, this project terminated and a follow-on project (AFOSR FA9550-07-1-0048) was initiated at TAMU to complete the work of the original proposal. This report describes activities and results of the first 25 months. Therefore, it includes only a description of the random roughness experiments and a description of the incomplete work on the first objective, decomposing experimentally measured data into modes of the OSS continuous spectrum.

The random roughness portion of the study is accomplished by numerically generating quasi-random rough surfaces and manufacturing these surfaces using rapid-prototyping technology. Measurements of the disturbances that the rough surface creates in a Blasius boundary layer are obtained for three test configurations corresponding to roughness-based Reynolds numbers of $Re_k = 164$, 227 and 301. The two lower values give laminar flow; the highest value results in localized transition approximately 140 mm downstream of the leading edge of the roughness. All three configurations exhibit transient growth of steady disturbances. Unsteady fluctuations indicate that transition in the $Re_k = 301$ configuration is likely an example of a bypass transition mechanism in which the unsteady disturbance growth outpaces the stabilizing relaxation of the steady flow. Measurements above the roughness surface in the $Re_k = 227$ configuration provide a phenomenological model for distributed receptivity.

---

[1]Present affiliation: Department of Aerospace Engineering, Texas A&M University, College Station, TX, 77843-3141

The decomposition portion of the study is incomplete; work is continuing as part of the follow-on project at TAMU. To date, efforts have focused on collecting and analyzing flow disturbance data in the wake of a regular spanwise array of cylindrical roughness elements. Measurements are obtained of the steady U' (streamwise) and W' (spanwise) disturbances and these are used to generate estimates of V' (wall normal). Because the W' velocities are small and $\partial U'/\partial x$ is small, estimates of V' have proved to be unreliable and, in fact, difficulties have been encountered in realizing appropriate disturbance boundary conditions. Thus, a straightforward decomposition approach using the biorthogonal eigenfunction system has been unsuccessful. As an alternative, ongoing work will explore a Monte Carlo–based approach.

As part of the effort to verify earlier results regarding disturbances generated by regular roughness arrays, a set of experiments duplicating earlier work were performed. These experiments have helped to reveal the role of Re_{δ_k} on the sub-optimal transient growth process.

The results of the experiments are available in the following published and forthcoming papers and student theses:

- Ergin, F.G. 2005. *Roughness Induced Transition*, Ph.D. dissertation, Case Western Reserve University.

- White, E.B., R.S. Downs III and H.C. Emer. 2006. Disturbances generated by random and period surface roughness: Experiments and models (invited). *AIAA Paper 2006-3526*.

- Ergin, F.G., and E.B. White. 2006. Unsteady and transitional flows behind roughness elements. *AIAA Journal* **44**(11):2504-2514.

- Downs, R.S., III. *Receptivity and Transient Growth of Disturbances Generated by Random Distributed Roughness*, M.S. thesis, Case Western Reserve University, 2007.

- Downs, R.S. III, E.B. White, and N.A. Denissen. 2008. Transition induced by random distributed roughness. *AIAA Journal* **46**, to appear.

- Denissen, N.A., and E.B. White. 2007. Roughness induced bypass transition, revisited. *AIAA Journal*, submitted.

The project involved one faculty member, two graduate students and two undergraduate students. The project P.I. was Edward B. White, an associate professor in the Department of Mechanical and Aerospace Engineering at Case Western Reserve University. The two graduate students were F. Gökhan Ergin and R. S. Downs III. Dr. Ergin earned his Ph.D. degree through research on this project and continued for one semester as a post-doctoral fellow. He is now employed by Dantec Dynamics, a manufacturer of fluid mechanics research instrumentation. Mr. Downs earned his M.S. degree through research on this project. He is continuing toward his Ph.D. degree at Texas A&M University with follow-on AFOSR support. One undergraduate student from Case Western Reserve University, Nicholas Denissen, has graduated with a B.S. in Aerospace Engineering and is continuing to perform AFOSR-funded research as a graduate student at Texas A&M University. The other undergraduate student, Sanjeeb Bose, graduated from CalTech and is continuing to graduate school at Stanford University.

Contents

List of Figures

Final Report for AFOSR Grant FA9550-05-1-0048

Experiments on the Receptivity of Transient Disturbances to Surface Roughness and Freestream Turbulence

Edward B. White[1]

Department of Mechanical and Aerospace Engineering
Case Western Reserve University
10900 Euclid Ave.
Cleveland, OH 44106-7222

1 Introduction and Objectives

1.1 Background

The stability of boundary layers has been analyzed most successfully using a normal mode decomposition of the Navier–Stokes equations linearized about a steady basic state. Using this approach, a flow is considered unstable if any of its disturbance modes are subject to exponential growth or stable if all of its modes are subject to exponential decay. This analysis leads to the familiar Orr–Sommerfeld/Squire (OSS) equations that can be solved using either a temporal or spatial formulation. The solution describes the growth and decay of Tollmien–Schlichting (TS) waves at various Reynolds numbers, wave numbers and frequencies. For 2-D boundary layers, Squire's Theorem gives the well-known result that 2-D, streamwise-traveling disturbances (i.e., those with spanwise wavenumber $\beta = 0$) are destabilized at lower Reynolds numbers than obliques waves, and consequentially, most of the work done to date on this system has focused on the growth of these 2-D waves because they have been viewed as the most important to the transition process.

While this approach successfully describes the boundary layer when the initial disturbance amplitudes are very low, a number of important problems that include high-amplitude freestream turbulence, high-amplitude surface roughness, or both, undergo a transition process that includes disturbance growth in regions where the Reynolds number is small and all the normal modes are subject to exponential decay. This phenomenon was named *bypass transition* because the disturbances were said to bypass the well-understood TS route to turbulence. For many years bypass was attributed to unknown nonlinear interactions of the disturbance modes, not because of any direct evidence of such interactions, but rather because the transition mechanism in those cases defied any other explanation (Reshotko 2001).

A relatively recent development that addresses the bypass transition problem is a theory known as *transient growth*. Transient growth is an attractive theory because it appears to be capable of explaining many subcritical (i.e., subcritical to the growth of TS waves) transition phenomena of heretofore unknown origin, especially those involving spanwise-varying disturbances, exactly the sort of disturbances produced by surface roughness or freestream turbulence. Transient growth is fundamentally different than TS wave growth because it results from an *inviscid* rather than a viscous mechanism and produces *algebraic* rather than exponential growth. Disturbances that experience this algebraic transient growth eventually decay exponentially, but prior to this decay they are capable of undergoing

---

[1]Present affiliation: Department of Aerospace Engineering, Texas A&M University, College Station, TX, 77843-3141
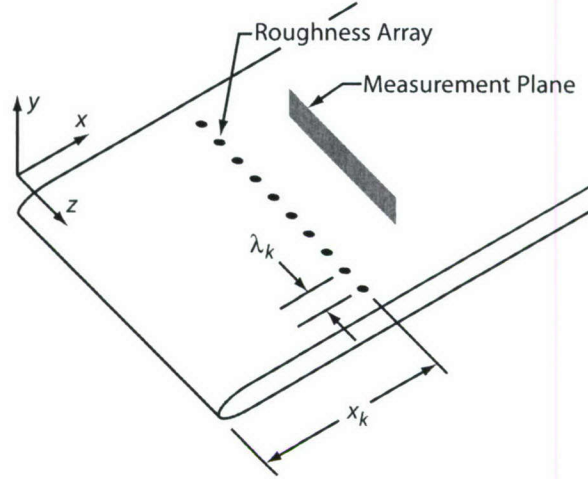
Figure 1: Coordinate system, roughness array parameters and measurement plane orientation.

very significant growth and should therefore be considered to be equally likely as TS waves to lead to transition. Despite the original suspicion to the contrary, transient growth is a linear mechanism.

Within the context of classical stability analysis, basic results include the minimum critical Reynolds number and the exponential growth rate, wavenumber, and frequency of the most unstable disturbance. This type of result is not appropriate for transient growth studies because transient growth occurs even when all eigenmodes are damped and there are no unstable modes. Instead, a concept introduced by Farrell (1988) is to examine the initial value problem in an optimization context and find the initial disturbance that produces the maximum disturbance kinetic energy at a specified later time. Studies by Butler and Farrell (1992) and later studies by Andersson et al. (1999), Luchini (2000) and Tumin and Reshotko (2001) have identified that the optimal disturbances in Blasius boundary layer are stationary, streamwise-oriented vortices that evolve into streamwise streaks. The wavenumbers for the optimal disturbances are $\alpha = 0$, $\beta = 0.45$ where β is made dimensionless using the boundary-layer scale, δ.

Prior to the previous AFOSR project (FA9620-02-1-0058), no experiments had been performed to deliberately examine whether transient growth of stationary disturbances occurs or whether roughness generates transient disturbances. Some evidence suggested that roughness can lead to transient growth (Tani et al. 1962; Reshotko and Leventhal 1981; Kendall 1981) but none of relevant experiments were conducted in a way that could conclusively verify this idea.

1.2   Results of previous AFOSR-funded experiments

Working from this background, the previous experiments sought to deliberately examine whether surface roughness produces transient disturbances. And, if it does, whether these disturbances grow and decay in a manner consistent with optimal-growth predictions. A variety of experiments were conducted using cylindrical roughness elements arranged in a spanwise-oriented array some distance downstream of the leading edge of a flat plate, x_k. The plate was oriented to provide a low-speed, zero-pressure-gradient Blasius boundary layer. The roughness heights, k, and spanwise spacings, λ_k, were systematically varied to determine the effects of these parameters on the resulting disturbances. Also varied was the ratio between the roughness elements' diameters, D, and the roughness elements' spanwise spacing. A sketch of the experimental setup is shown in Fig. 1.

A number of key findings resulted from the prior experiments. These are principally reported by White (2002), White et al. (2005) and Ergin and White (2006). First, White (2002) establishes that spanwise arrays of 3D roughness elements do indeed generate stationary disturbances that undergo transient growth. This was the first experiment to verify this conclusively. However, the experiment also revealed that roughness-induced disturbances are not optimal. Some general features of optimal disturbances can be observed for roughness-induced disturbances. But, optimal-disturbance theory overestimate the streamwise length over which growth occurs and also overestimates the total amount of growth. White (2002) links the discrepancy between the theoretical predictions and the experimental observation to receptivity. That is, the process by which the roughness generates an initial disturbance distributes energy across the continuous OSS spectrum in a way that differs from the optimum distribution.

In order to better understand receptivity issues, White et al. (2005) conducted detailed studies that varied Re_k and D/λ_k for a roughness array at a fixed x_k and unit Reynolds number, Re'. The experiments focused on the role of Re_k varied this parameter between values of 16 and 195 while maintaining $D/\lambda_k = 1/3$. For this configuration, certain spanwise modes undergo clear transient growth, the modes whose wavelengths are $\lambda_k/3$ and $\lambda_k/4$, in particular. However, the λ_k mode shows only weak growth after a dramatic initial decay; the $\lambda_k/2$ mode only decays. Again, the key conclusion is that the distribution of initial disturbance energy amongst the relevant continuous modes is critical to the nature and magnitude of the transient growth. Moreover, no realizable disturbance appears to be optimal.

White et al. (2005) observe that as Re_k is varied, the energy associated with each of the modes, E_λ, and with the total stationary disturbance, $E_{\rm rms}$, scales as Re_k^2. This scaling is observed to be valid across the entire range of Re_k values examined in the experiment. Typical results of this experiment are shown in Fig. 2 which gives the disturbance energy of the $\lambda_k/3$ spanwise mode for various Re_k values. The curves in Fig. 2 are fits to the empirical function

$$E_{\lambda_k/3}(x) = a\,(x - x_k) \exp\left(-\frac{x - x_k}{b}\right)$$

where a and b are fitting parameters. For these data, $a = A\,Re_k^2/\delta_k$ where $A = (4.3 \pm 0.2) \times 10^{-9}$. This establishes the Re_k^2 energy scaling. The decay length b is a weakly increasing function of Re_k. Experiments that vary D/λ_k at fixed Re_k established extreme sensitivity of the magnitude and even qualitative nature of the transient growth to small changes in the roughness configuration.

The data presented by White et al. (2005) only extend to $Re_k = 195$ because beyond that value, bypass transition occurred; Rice (2004) observed bypass at $Re_k = 254$. To examine the nature of this bypass transition, Ergin and White (2006) extended the Re_k range to $Re_k = 339$ and made a detailed study of the steady and unsteady flow at subcritical and this supercritical Re_k. Those experiments revealed unsteady u' fluctuations in the roughness elements' wakes that grow while the U' disturbance is large. The most significant growth is associated with regions of large $\partial U'/\partial z$ gradients. The u' growth is exponential and is thus thought to be the result of a Kelvin–Helmholtz-type instability; it is not transient growth of unsteady disturbances. Once the U' disturbance has sufficiently decayed, the u' disturbances decay as well. At $Re_k = 202$ and 264, the initial U' disturbance is sufficiently small that the flow becomes stable to growing u' disturbances before they grow to large amplitude. However, in the supercritical case, the u' amplification rates are higher and persist for a longer streamwise distance. This gives the unsteady disturbances the ability to grow and bring about transition before they stabilize.
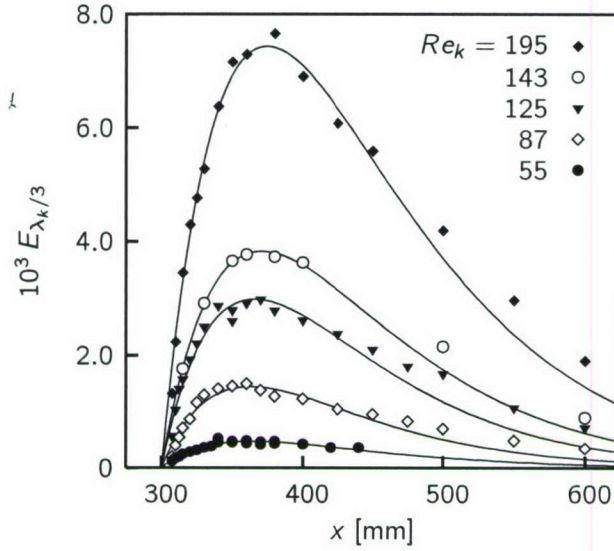
Figure 2: Variation in the $E_{\lambda_k/3}$ disturbance energy across varying Re_k for $D/\lambda_k = 1/3$.

After the bypass experiments by Ergin and White (2006) were completed, a DNS of the setup was performed by Rizzetta and Visbal (2007). Those computations confirmed the basic transition mechanism identified by Ergin and White. However, the DNS found that for the supercritical case, $Re_k = 339$, transition occurs much farther downstream in the experiment than it does in the computation. Also, the computation shows significantly more fine-scale disturbance detail than does the experiment. Thus, there is some concern that the Re_k values reported by Ergin and White (2006) might have been incorrect. If the reported values were lower than the actual values, this would result in the discrepancies between the DNS and experimental results.

1.3   Objectives

The present project, AFOSR Grant FA9550-05-1-0048, follows the previous experiments funded by AFOSR Grant FA9620-02-1-0058. Thus, the present work focuses on receptivity of transient disturbances as receptivity has been identified as being critical to the transient growth phenomenon. The work is intended to address both roughness- and freestream-turbulence-induced disturbances and to address both regular and random disturbances.

There are three specific objectives of the present project. First, a technique is to be developed to permit a rigorous decomposition of measured steady disturbances across the continuous spectrum of Orr–Sommerfeld/Squire (OSS) eigenmodes. This technique would bridge the gap between the experimental observations of non-optimal growth and optimal-growth predictions by quantifying the contribution of each continuous-spectrum mode. Second, the receptivity and transient growth of steady disturbances generated by quasi-random distributed surface roughness are to be investigated. Real surfaces include random roughness and, therefore, it is of interest to determine if and how knowledge about discrete 3D roughness can be extended to real surfaces with distributed, random roughness. Third, transient disturbances generated by controlled freestream turbulence are to be investigated. Turbulence is thought to generate unsteady transient growth (Reshotko 2001; Schmid and Henningson 2001) and it is of interest to make detailed measurements of those disturbances as well.

This report describes activities and results of the first 25 months of work originally proposed for a 36-month period. The project was canceled after 25 months when the PI, Prof. Edward White, moved from Case Western Reserve University to Texas A&M University. During the first 25 months, the second objective, examining the receptivity to random, distributed roughness was successfully achieved. Work on the first objective, decomposing experimental data into a spectrum of continuous OSS eigenmodes was intended to continue throughout the entire project and thus remains incomplete. Parts of that objective have been achieved. Work on the third objective did not begin at Case. The remaining work has been reinitiated at Texas A&M University under AFOSR Grant FA9550-07-1-0312. The following sections describe the general experimental approach and progress toward the first objective and the completed work on the second objective.

2 Experimental Approach

2.1 Wind tunnel, instrumentation and flat plate model

The wind tunnel facility used for the experiments is the Case Western Reserve University (Case) wind tunnel, an open-return facility with a 710 mm × 710 mm × 2.7 m test section and a maximum operating speed of 25 m/s. The tunnel's design follows the recommendations of Reshotko et al. (1997) for flow quality. Operating at 12 m/s, the total (not high-pass-filtered) u'_{rms} level in the test section is approximately 0.35% U_∞. Although this level may seem high relative to other tunnels, fluctuation spectra indicate that approximately 93% of the fluctuation power is contained below 1 Hz, a conservative cutoff frequency for AC-coupling filters. To compare the fluctuation measurements of the Case tunnel to facilities whose quoted turbulence levels are measured using traditional AC-coupled fluctuation-intensity measurements, only the u' intensity above 1 Hz should be considered. Restricted to these frequencies, the Case tunnel's u'_{rms} level is 0.09% U_∞. Alternatively, separating the contributions of acoustic and turbulent velocity fluctuations in the manner suggested by Reshotko et al. (1997) shows that the turbulent u'_{rms} amounts to 0.05% U_∞.

Velocity measurements are made using two 2.5-μm-diameter hotwire probes. Streamwise velocity measurements are made concurrently in the boundary layer and the freestream. The velocity measured by the boundary layer probe is normalized on a point-by-point basis by the freestream velocity U_∞ to give a nondimensional boundary layer velocity. Measurement of the flow field is accomplished by collecting data in dense 2D grids at varying streamwise locations. The motion of hotwire probes is controlled by an externally mounted traverse that provides approximately 1200 mm of travel in the streamwise direction (x), 190 mm of travel in the spanwise direction (z) and 70 mm of travel in the wall-normal direction (y). The stepper motors that drive the traverse provide this motion in steps of 3.2 μm, 1.6 μm and 1.6 μm, respectively.

The flat plate model used here was originally constructed by Reshotko and Leventhal (1981). The model is mounted vertically in the tunnel 0.5 m downstream of the test section inlet, with the test side located approximately 250 mm from test section's side wall. The plate is constructed of aluminum and is 9.5 mm thick, 635 mm in span, and 1100 mm in length. The plate's leading edge is elliptical with the flat portion of the plate beginning 25 mm from the leading edge. A hinged trailing-edge flap is used to ensure that the incoming flow stagnates on the test side of the plate. The test side of the plate is polished to a near-mirror finish.

During previous experiments (e.g., White 2002; White et al. 2005), arrays of discrete roughness elements were attached directly to the plate surface (see Fig. 1). For all of the experiments of the present experiments a different approach was used. Studying random roughness was of interest during
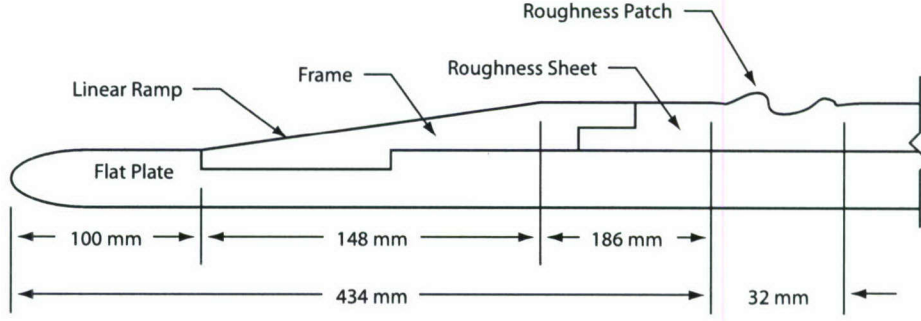
5

Figure 3: Schematic diagram of the flat plate, roughness sheet and aluminum frame. Not to scale.

these experiments and manufactured roughness sheets are used for this purpose. (More details on the roughness design and manufacture are given in Sec. 3.1.) The manufactured sheets were 230 mm by 230 mm in their streamwise and spanwise dimensions and 6 mm thick with a 3-mm-thick, 12-mm-wide border extending beyond the nominal 230 mm by 230 mm extent.

In order to attach the roughness sheets to the flat plate, an aluminum frame was constructed. The frame has two purposes. It secures the roughness sheet to the plate and provides a smooth ramp from the plate surface to the roughness surface. Figure 3 is a schematic diagram of the frame and roughness sheet with roughness characteristic of the experiments described in Sec. 3. The front portion of the frame sits in a shallow recess in the flat plate surface that has been used to hold recessed sandpaper for similar experiments (White and Reshotko 2002). Here it allows a continuous interface between the plate and the frame while maintaining a suitably thick frame leading edge. The leading edge of the frame's linear ramp begins 100 mm downstream of the plate's leading edge; its thickness increases to the roughness sheet's thickness over a distance of 148 mm. Immediately aft of the ramp is a 186-mm-long smooth, flat section that is blended to the leading edge of the roughness sheet using a epoxy filler that is sanded smooth. The junction at the trailing edge of the roughness sheet is treated similarly. The trailing edge of the aluminum frame as well as its sides are blunt; no attempt is made to provide a continuous interface between the frame and the plate surface at those edges. Additional details regarding this setup are available in Downs (2007).

Further details about the experimental arrangement are specific to the individual experiments and will be discussed in the appropriate sections.

2.2 Hotwire measurement techniques and data analysis

Measurements are performed by hotwire anemometers that are moved through spanwise–wall-normal planes oriented as shown in Fig. 1 at various x locations. An integer number of z steps is performed per λ_k; this permits spatial phase-lock averaging to be performed on the data in order to minimize random variations in the steady velocity field.

Streamwise velocity measurements are obtained using straight-wire probes and are decomposed into a spanwise-invariant basic state, a stationary disturbance and an unsteady disturbance as

$$u(x, y, z, t) = \overline{U}(x, y) + U'(x, y, z) + u'(x, y, z, t).$$

The basic state profile $\overline{U}$ is computed by spanwise phase-locked averaging the steady velocity profiles measured at z locations that are judged to be outside the influence of upstream roughness. This

averaged profile is expected to be least affected by the roughness and most representative of Blasius flow.

Boundary-layer integral quantities, δ^* and θ are computed from basic-state profiles at each x and these measurements are used to verify the plate's alignment for zero pressure gradient and to nondimensionalize the wall-normal coordinate as $\eta = y/\delta$. First, a zero-pressure-gradient condition is verified by the shape factor $H = \delta^*/\theta$ falling in the range 2.59 ± 0.05 (Saric 2007). If this is verified, the boundary-layer thickness scale δ is given by $\delta = \delta^*/1.7208$ and $\delta = \theta/0.664$. For each experimental configuration, a nonlinear least squares fit is performed to the $\delta(x)$ data resulting from both δ^* and θ as

$$\delta(x) = \left(\frac{x - x_{\text{v.l.e.}}}{Re'} \right)^{1/2}$$

where the fit parameters are $x_{\text{v.l.e.}}$, the virtual leading edge location, and Re', the unit Reynolds number, U_∞/ν. Uncertainties are known for the experimental δ values so uncertainties are computed for the fit parameters. Applying these values allows calculation of boundary-layer and roughness parameters and those parameters' uncertainties at any x location.

Because spanwise-periodic roughness is used, even in the random roughness cases, velocity profiles measured aft of the roughness are also phase-locked averaged using the periodicity λ_k. This process results in a representative flow field for one roughness array length. The steady boundary layer disturbance is defined as the deviation from the basic state. Thus, the steady disturbances $U'(\eta, z)$ are computed by subtracting the basic state profile from each of the other averaged profiles obtained behind the roughness. To collapse this steady disturbance field to a single profile that is representative of the overall flow disturbance the roughness creates, the root-mean-square of the steady disturbance profiles is taken in the spanwise direction. The result is a single disturbance profile, $U'_{\text{rms}}(\eta)$. The total disturbance energy, E_{rms}, is quantified as the wall-normal integral of this profile squared:

$$E_{\text{rms}} = \int_0^\infty [U'_{\text{rms}}(\eta)]^2 \, d\eta.$$

In practice, this integration is carried out using a simple trapezoidal integration scheme. The upper limit of integration is in the freestream where the disturbance profile is close to zero. Typically, η values of 10 to 12 are used for this purpose.

Although the total disturbance energy is a useful means of quantifying the streamwise disturbance evolution, it gives no information as to the behavior of individual spanwise wavelengths in the velocity disturbance field and how these wavelengths might be connected to the roughness. To examine these details, the $U'(\eta, z)$ disturbances are transformed using a spatial Fourier transform in the spanwise direction. This operation is completed using two roughness patches as a spanwise sampling length. Overlapping four such transforms by 50% and complex-averaging the results achieves the optimal reduction in the variance (Press et al. 2001).

After performing the Fourier transforms, the power spectral density (PSD) of the signal is computed. The normalization is such that:

$$[U'_{\text{rms}}(\eta)]^2 = \sum_{m=0}^\infty \text{PSD}_m(\eta).$$

The disturbance energy contained in any particular mode can be found in a manner similar to the total disturbance energy. The PSD component of interest is integrated in the wall-normal direction using a
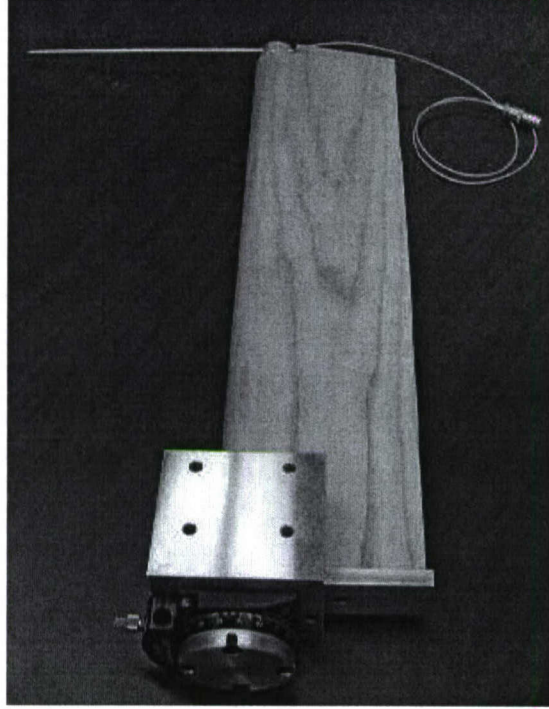
Figure 4: Multiple-probe hotwire sting with angular adjustment capability.

simple trapezoidal scheme:

$$E_{\lambda_k/m} = \int_0^\infty \text{PSD}_m(\eta)d\eta.$$

As a consequence of the PSD normalization, the total disturbance energy is equal to the sum of the disturbance energies in each of the integer modes:

$$E_{\text{rms}} = \sum_{m=0}^\infty E_{\lambda_k/m}.$$

Spanwise velocity measurements are obtained using a pair of slant-wire probes with different angular orientations at the same location. For this purpose, a new hotwire sting design is used that carries a combination of slanted and straight hotwire sensors (Fig. 4). This sting assembly includes a shaft that rotates in a streamlined casing and allows angular calibration of slanted hotwires. Outside the test section, the shaft is connected to an angle indicator and the sting assembly is rigidly attached to the traverse. Inside the test section, the hotwire sensors are placed perpendicular to the shaft's axis through a multiple-hotwire holder. The angular position of the sensors can be adjusted by rotating the spindle of the angle controller with a precision of $0.2°$. The multiple-hotwire holder is designed to carry four hotwires. One hotwire is a straight sensor in the freestream; the remaining three sensors are in the boundary layer. The boundary-layer sensors are positioned in a trident design with one straight sensor in the middle and two slanted hotwire sensors mounted 9.5 mm one either side of the the center probe. Using a separation that is an integer multiple of the spanwise step permits all three boundary layer sensors to be placed at the same measurement location at three different spanwise traverse steps. Naturally, this requires excellent alignment of the flat surface with the traverse plane and the sensors with respect to each other and great care is exercised to achieve this alignment.

Sensor	A	B	k	n
Freestream	−1.591	0.582	2.258	−
Boundary Layer	−1.419	0.538	2.377	−
Top Slanted	−1.546	0.551	2.328	0.160
Bottom Slanted	−1.879	0.665	2.209	0.180

Table 1: Typical calibration constant values obtained during multicomponent experiments.

Slanted hotwire angle calibration is performed following the recommendations of Bruun (1995). First, the yaw angle of each wire is determined by gradually rotating the sensor in the freestream and monitoring the bridge voltage. When the bridge voltage is a maximum, the maximum cooling rate is achieved because the impinging velocity is perpendicular to the wire axis. The calibration of all four sensors is performed simultaneously. First, the sting is positioned so that all hotwires are located in the freestream. Second, it is rotated 5° clockwise from its position during an experiment and a velocity calibration is performed. Third, the sting is rotated 10° counterclockwise and another velocity calibration is performed for the same tunnel speed range. Finally, data from both velocity calibrations at two different angles are combined and the calibration constants are computed by using the King's Law and Hinze's formula (Hinze 1959):

$$V_e = \left(A + B E^2 \right)^n = \tilde{V} \left(\cos^2 \alpha + k^2 \sin^2 \alpha \right)^{1/2}.$$

In these equations A, B and n are calibration constants, $\tilde{V}$ is the freestream speed (during the calibration procedure only), V_e is the effective cooling velocity, E is the hotwire voltage, α is the sensor's yaw angle and k is the sensor's yaw coefficient. A nonlinear least-square fit is performed to find A, B, n and k values for each sensor. The yaw coefficient is assumed to be constant following Jørgensen (1971). According to Bruun, this method predicts the effective cooling velocity to within 1% for yaw angles between 0° and 70° and the error reaches only 15% for a yaw angle of 90°.

In the present work, alignment tests showed the slant-wire α values to be $40.0° \pm 0.5°$. Typical values for the Hinze-formula constants are give in Table 1. Precise determination of the yaw coefficient, k requires a very accurate knowledge of the wire angle, α. Typical k values for single yawed sensors reported in the literature are around 0.1. According to a study cited by Bruun (1995), the value of the calculated yaw coefficient k^2 is very sensitive to an assumed yaw angle error, σ_α; a yaw-angle uncertainty as low as 1° can produce negative values for k^2, which is note physically possible. As noted above, the present yaw-angle uncertainty is 0.5°. There could, therefore, be considerable errors in k. Fortunately, the individual uncertainties from α and k cancel in Hinzes formula, reducing the combined uncertainty on the right-hand-side to less than 1%.

3 Distributed Roughness Experiments

Previous experiments on transient disturbances induced by surface roughness have focused on spanwise-periodic arrays of geometrically simple roughness elements (White 2002; Fransson et al. 2004; White et al. 2005). This approach provides a clear connection between the experiments and stability theory. However, connecting these experiments to more realistic situations requires the study distributed roughness effects that is characteristic of what would be encountered on actual aircraft surfaces.

The experiments presented here provide data intended to help incorporate randomly distributed

3D surface roughness into a theoretical framework. The approach is to manufacture a surface whose coordinates are randomly generated and to observe how disturbances are generated by this surface, how they grow and how they bring about transition. There are numerous advantages associated with manufacturing random rough surfaces. These include the ability to reproduce experimental conditions in other experiments and in numerical simulations, as well as the ability to know and control key features of the rough surfaces parameters for comparisons with theoretical models. There are also distinct experimental advantages to this approach. For this work, the roughness is spatially extended but most growth measurements are made over a smooth surface downstream of the roughness. This is a necessary first step that avoids the complication of combined disturbance growth and distributed disturbance accumulation over the roughness. Additionally, however, some measurements are made over distributed roughness and these provide clues as to the nature of distributed roughness receptivity.

The experiments are performed in the Case Western Reserve University wind tunnel, a low-speed open-return tunnel. Realistic surface roughness is approximated using a spanwise-periodic array of roughness patches. Rapid prototyping technology is used to manufacture a sheet of roughness that is incorporated onto a flat plate. Streamwise velocity measurements are made downstream of and over the surface of the roughness. These measurements are used to determine how the steady disturbances are generated by the roughness and how they evolve in the streamwise direction.

Three different roughness-based Reynolds numbers Re_k are investigated. As a single sheet of roughness is used, Re_k is changed by varying the freestream velocity. The three test configurations utilize freestream speeds of 7.5, 9.3 and 11.5 m/s which correspond to Re_k values of 164, 227 and 301, respectively. These values are based on the undisturbed boundary layer thickness at the roughness location and the maximum roughness height. The $Re_k = 164$ and 227 cases are fully laminar while the $Re_k = 301$ case becomes turbulent approximately 180 mm downstream of the roughness elements.

3.1 Roughness design and implementation

Spanwise-periodic, quasi-random roughness is used to mimic real surface roughness. Previous experiments (White 2002; White et al. 2005) that used spanwise arrays of cylindrical roughness elements found spanwise periodicity to be useful for spatial phase-locked averaging of the velocity measurements. To achieve spatial periodicity here, a roughness array with seven identical patches of roughness is designed. Of these seven, five are in the range of the hotwire traverse; the two outside patches ensure periodicity. Given the spanwise range of the hotwire traverse (190 mm), the roughness array wavelength λ_k is selected to be 32 mm. The roughness patches are designed to contain the fundamental wavelength λ_k and its first ten harmonics. The streamwise length of each roughness patch is also limited to 32 mm. Relative to the physical leading edge of the flat plate, the roughness extends from $x = 434$ mm to 466 mm in the streamwise direction; the streamwise midpoint ($x = 450$ mm) is denoted as x_k. This range of x locations corresponds to boundary-layer-scale Reynolds numbers of $Re_\delta = 452$ to 470, 533 to 543 and 626 to 638 for the three test cases, $Re_k = 164$, 227 and 301, respectively. These values all fall above $Re_\delta = 302$, the minimum critical Reynolds number for TS wave growth. Thus, it is possible that TS waves are growing in the experimental domain.

The Blasius boundary layer has an optimal disturbance whose dimensionless spanwise wavenumber β is 0.45 (Andersson et al. 1999; Luchini 2000; Tumin and Reshotko 2001). Based on the boundary layer thickness at the streamwise midpoint of the roughness $\delta_k = [(x_k - x_{v.l.e.})/Re']^{1/2}$, λ_k corresponds to $\beta_k = 0.17$ for the $Re_k = 227$ case. That is, the roughness patches are periodic over a length that is about three times the optimal wavelength. Thus, $m = 3$ is the spanwise mode that is closest to the optimal spanwise wavelength. For the $Re_k = 164$ configuration, $\beta_k = 0.19$; for the $Re_k = 301$

Table 2: The largest amplitude values (normalized) and associated indices

$A_{n,m}$	n	m
1	3	4
0.953	4	4
0.901	8	4
0.801	1	2
0.684	4	3
0.661	1	1

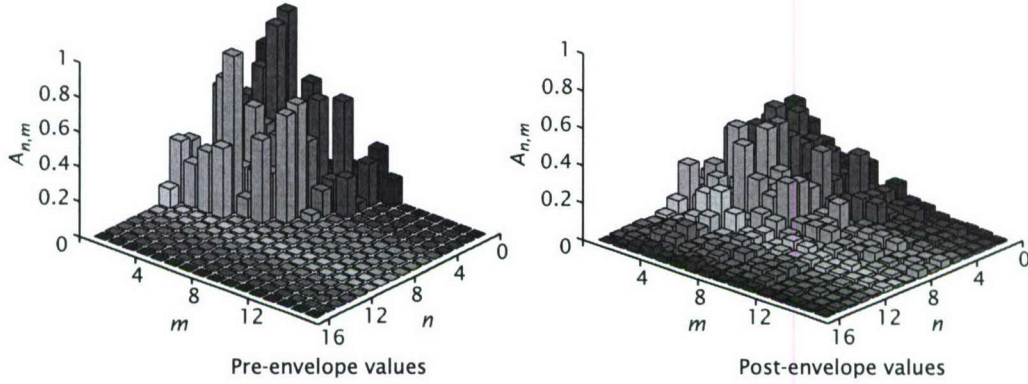Pre-envelope values   Post-envelope values

Figure 5: Normally distributed amplitude coefficients not including the envelope function (left) and including the envelope function (right)

configuration, $\beta_k = 0.16$.

A randomly rough surface is modeled as a series of cosine functions with randomly distributed amplitudes $A_{n,m}$ and phases $\phi_{n,m}$ that are chosen from normal and uniform distributions, respectively. Thus, the surface height with respect to the plate surface is given by

$$h(x, z) = \sum_{n=1}^{N} \sum_{m=1}^{M} A_{n,m} \cos(2\pi nx/\lambda_k + 2\pi mz/\lambda_k + \phi_{n,m})$$

where $N = M = 10$. To limit the minimum roughness wavelength to $\lambda_k/10$, amplitude coefficients with $n^2 + m^2 > 10^2 + 1$ are set to zero. A graphical representation of the amplitude coefficients is shown in Fig. 5. The largest amplitude values are summarized in Table 2. The top three values correspond to the $m = 4$ spanwise component; this is not intentional but rather a result of the random selection process.

It is desired that the roughness elements not cause a bypass transition at a nominal freestream speed of 10 m/s. Previous transient growth experiments (White and Ergin 2003) have shown that the elements should not exceed $Re_k = 250$ and this corresponds to a maximum roughness height of about 1 mm at the roughness location. The thickness resolution of the rapid prototyping process is 0.1 mm so the surface is reasonably well resolved.
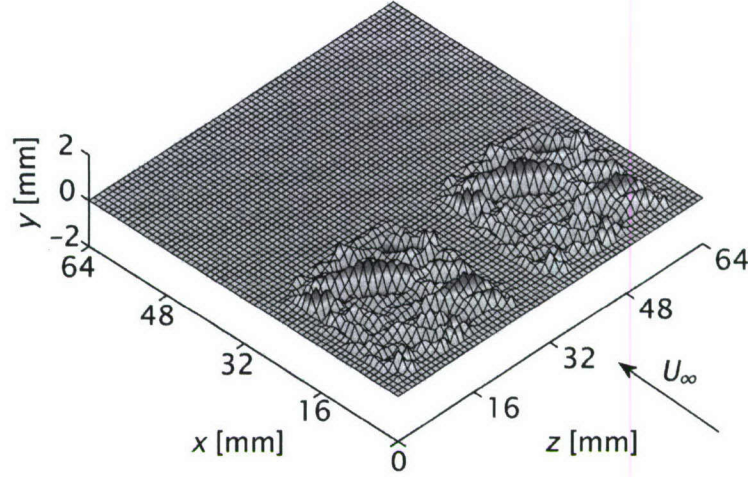
Figure 6: Numerical representation of two patches of roughness

Table 3: The largest post-envelope amplitude values and associated indices

$A_{n,m}$	n	m
0.469	4	3
0.435	5	4
0.433	6	4
0.395	1	2
0.393	8	4
0.393	2	3

An additional feature that is incorporated into the roughness is a series of 4-mm-wide flat strips that run in the streamwise direction. These so-called roughness flats are included to provide regions in the flow where the steady disturbance from the Blasius state, U', is small. These locations are used to estimate the wall location in traverse coordinates using linear least squares fits to the wall. As shown by White and Ergin (2004), linear fits cannot be used directly behind roughness elements; the roughness flats are critical to this approach. The roughness flats are also used to measure the experimental basic state of the boundary layer. To generate the flats, each roughness patch is multiplied by an envelope function in both the streamwise and spanwise directions. In addition to providing the 4 mm of smooth space between each patch, the envelope function also provides a 4-mm-wide cosine ramp into and out of the rough surface. A schematic drawing of two patches of the numerically generated surface roughness is shown in Fig. 6.

One unintended consequence of applying the envelope function to the roughness is a partial loss of the intended wavelength cutoff. The right side of Fig. 5 shows the amplitude coefficient values that result from the application of the envelope function. The top post-envelope amplitude values are summarized in Table 3; the values are normalized by the highest pre-envelope value. Although the envelope function does generate wavelengths shorter than $\lambda_k/10$, 65% of the amplitude content remains in the original longer-wavelength region ($n^2 + m^2 \leq 10^2 + 1$).
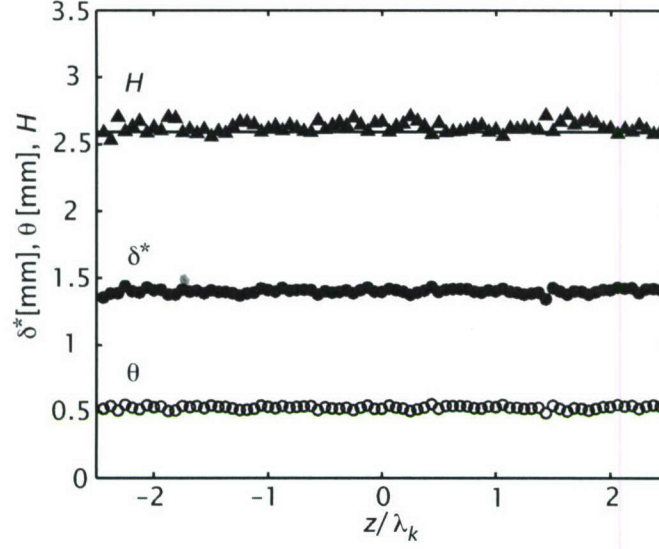
Figure 7: Boundary layer integral quantities at $x = 425$ mm

3.2 Alignment for basic state

In preparation for these experiments, the plate is aligned such that the streamwise-average value of the boundary layer shape factor H is 2.61 for a freestream speed of 9.3 m/s. This value falls within an acceptable range (Saric 2007) of the theoretical zero pressure gradient value, $H = 2.591$. At the same velocity, the virtual leading edge location $x_{v.l.e.}$ is found to be 78 ± 17 mm and the unit Reynolds number is computed to be $Re' = (513 \pm 22) \times 10^3$ m^{-1}. The uncertainties in these quantities are slightly larger than those quoted for previous experiments (e.g., White et al. 2005) due to the nature of this experimental setup. While it was possible in previous experiments to measure alignment data before the roughness elements were adhered to the flat plate (thus using the entire span for these measurements), alignment data for the present experiments could only be measured in spanwise locations where there was no roughness. As fewer data points were available for computing the values of $x_{v.l.e.}$ and Re', the respective uncertainties in these quantities are higher.

Boundary layer thicknesses and shape factor measurements are also used to ensure that the flow just upstream of the roughness is spanwise-uniform. In order to correctly quantify the effect of the roughness on the measured flow field, any disturbance generated by the interface of the roughness frame and the roughness sheet should be minimal. To ensure that this is true, boundary layer profiles are recorded at many spanwise locations for $x = 425$ mm (9 mm upstream of the leading edge of the roughness). Shape factors are computed from these profiles and shown in Fig. 7 shows these data. The variance of δ^*, θ and H are deemed to be acceptable and the slope of each of these variables across the span is negligible.

3.3 Distributed roughness results: Subcritical flow

The steady disturbance profiles $U'_{rms}(\eta)$ and the basic state profiles $\overline{U}(\eta)$ for the $Re_k = 227$ case are shown in the bottom right corner of Fig. 8 for $x^* = 27$, 82 and 164 ($x = 475$, 525 and 600 mm respectively). At $x^* = 27$, 9 mm aft of the trailing edge of the roughness, the maximum U' is approximately 0.08. This is the largest value observed for $Re_k = 227$; the disturbance magnitudes decrease with
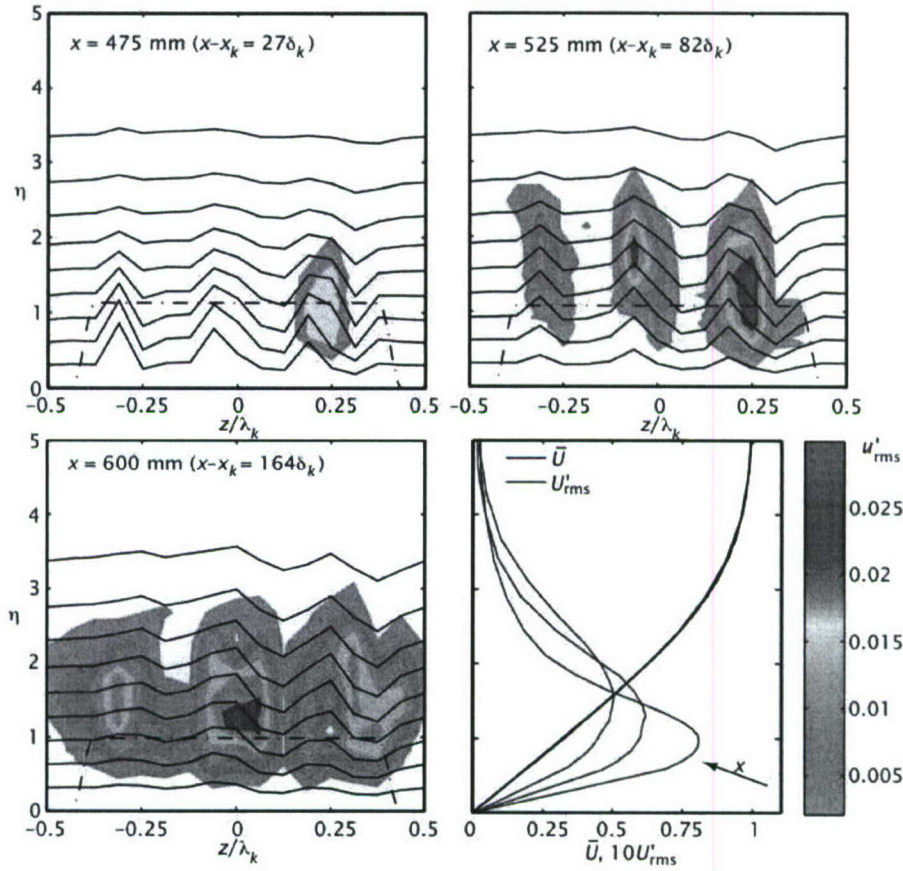
Figure 8: Velocity contours and fluctuation velocity field for $Re_k = 227$; basic state and steady disturbance profiles corresponding to the contour plots are shown in bottom right. Steady velocity contours are at increments of $0.1U_\infty$

increasing streamwise distance. At $x^* = 82$, the magnitude has fallen to about 0.06. At $x^* = 164$, the magnitude has fallen to approximately 0.05. However, as its maximum amplitude decreases the steady disturbance profiles broaden in the wall-normal direction as they move downstream. This broadening is accompanied by an increase in the vertical distance between the wall and the peak of the disturbance profile. These observations are consistent with measurements of stationary transient disturbances initiated by arrays of isolated roughness elements (White et al. 2005; White 2002).

Another useful perspective for visualizing the boundary layer disturbances is streamwise velocity contours in wall-normal/spanwise planes; such plots are shown in Fig. 8. These plots show iso-velocity contour lines for one phase-locked average disturbance field. The dashed lines represent a projection of the envelope function that gives the maximum roughness height. This projection is normalized by δ at all x locations. In addition to contour lines, the unsteady fluctuation velocity u'_{rms} fields are also shown in these plots as the color contours. These contours are not phase-locked-averaged but rather represent the middle roughness patch.

The top left corner of Fig. 8 shows the velocity contours at $x^* = 27$. As evident from the contour lines, the flow is decelerated in three distinct zones: near $z/\lambda_k = -0.32$, -0.07 and 0.18. Additionally,
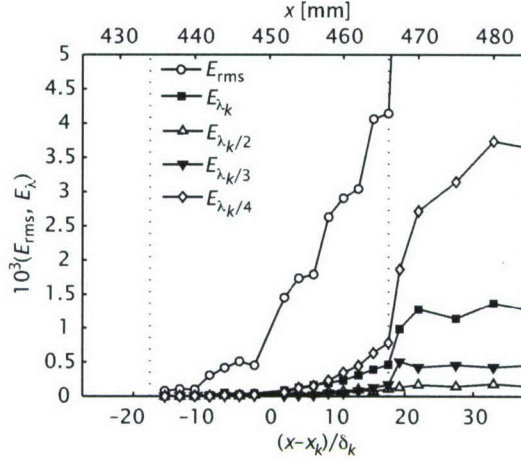
14

Figure 9: A selected portion of the disturbance energy evolution for $Re_k = 227$; the vertical lines indicate the receptivity region (the roughness surface)

the flow appears to be accelerated near $z/\lambda_k = 0.32$. Due to the spanwise juxtaposition of decelerated and accelerated flows in this region, there is a strong spanwise $\partial u/\partial z$ shear near $z/\lambda_k = 0.25$. This shear is accompanied by increased unsteady fluctuations as is evident in the color contours.

Similar behavior is observed at $x^* = 82$ (shown in the top right corner of Fig. 8). The three decelerated zones and single accelerated zone are persistent and are observed at the same z locations as they were upstream. In each case, the maximum disturbance amplitude has decreased while the disturbances have broadened away from the wall. While the U' disturbances decayed slightly, there has been significant u' growth about each of the three decelerated regions. This evolution continues at $x^* = 164$ (in the bottom left corner of Fig. 8) where the u' disturbances may have reached their maximum amplitude and are spreading out away from the originally decelerated zones. Similar to what was observed by Ergin and White (2006), the disturbed mean flow is initially unstable to growing u' fluctuations. However, the disturbances do not grow fast enough to lead to turbulence before U' relaxes to the point where the u' disturbances become stable.

The disturbance energies for the baseline $Re_k = 227$ case are shown in two plots: those measured over the roughness surface (Fig. 9) and the complete evolution downstream of the roughness (Fig. 10). The disturbances over the roughness are much smaller than those downstream and thus do not fit well on the same plot. Figure 9 shows the total disturbance energy and the disturbance energy in the first four spanwise modes as functions of x^*. The leading edge of the roughness starts at $x^* = -17.6$ and the first measurements are taken at $x^* = -15.4$. As this plot shows, the disturbance energy gradually increases up to the trailing edge of the roughness at $x^* = 17.6$. The disturbance energies in each of the first four spanwise modes increase essentially monotonically while E_{rms} seems to rise through a few quick bursts.

Figure 10 shows the total disturbance energy, E_{rms} and the disturbance energy in the first four spanwise modes, E_{λ_k}, $E_{\lambda_k/2}$, $E_{\lambda_k/3}$ and $E_{\lambda_k/4}$ as functions of streamwise distance downstream of the roughness surface. This plot shows the disturbance energy evolution above the roughness and aft of the roughness. E_{rms} undergoes an abbreviated period of transient growth and reaches its maximum 14 mm downstream of the trailing edge of the roughness at $x^* = 33$. From this point through the end of the measurement domain ($x^* = 164$), E_{rms} gradually decays. Its rapid growth from $x^* = 16.5$ to 33 can be almost completely attributed to growth in $E_{\lambda_k/4}$; both increase by approximately the same

15

x [mm]

440 460 480 500 520 540 560 580 600 620

$10^3 \langle E_{rms}, E_\lambda \rangle$

10
9
8
7
6
5
4
3
2
1
0

—○— E_{rms}
—■— E_{λ_k}
—△— $E_{\lambda_k/2}$
—▼— $E_{\lambda_k/3}$
—◇— $E_{\lambda_k/4}$

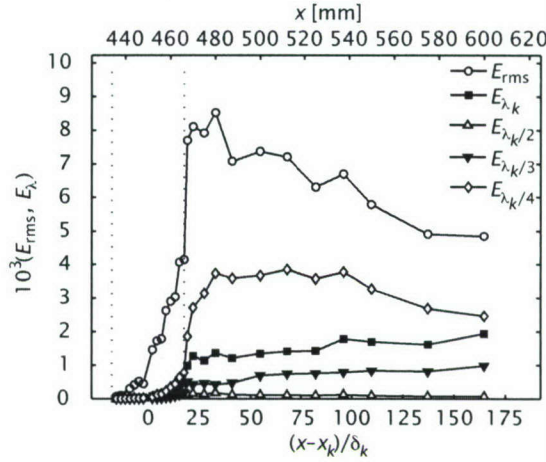0 25 50 75 100 125 150 175

$(x - x_k)/\delta_k$

Figure 10: The complete disturbance energy evolution for $Re_k = 227$; the vertical lines indicate the receptivity region (the roughness surface)

amount over this distance.

The λ_k disturbance energy exhibits relatively small transient growth over the length of the measurement domain. However, it grows throughout the domain and helps slow the decay of E_{rms} once $E_{\lambda_k/4}$ begins to decay. The $\lambda_k/2$ disturbance energy is quite small relative to the other components and does not appear to change in any significant manner. The $\lambda_k/3$ disturbance energy exhibits the same type of transient growth as the λ_k disturbance energy but at a somewhat lower rate. The most striking transient growth and corresponding decay is evident in the dominant $\lambda_k/4$ disturbance energy. This energy grows by a factor of four from its initial value to its maximum at $x^* = 33$. This period of transient growth is followed by decay over the remainder of the measurement domain.

One of the more notable features of Figs. 9 and 10 is the dramatic increase in disturbance energy and the disturbance energy growth rate that occurs at the trailing edge of the roughness. This could be seen as evidence that distributed roughness suppresses the transient growth of disturbances generated at the upstream portion of the rough surface. However, it is more likely that the discrepancy is due to a subtle change in experimental technique that is used for these two regions. When velocity measurements are made over the roughness surface, a high cutoff velocity is employed to reduce the possibility of physical contact between the hotwire probe and the roughness surface. For downstream measurements over the flat surface, a velocity cutoff of 20% of U_∞ is used. Once a velocity smaller than this is measured, the probe is moved away from the surface and to the next spanwise point. Over the roughness surface, a velocity cutoff of 42% is used. This value incorporates the boundary layer thickness in the receptivity region, the maximum roughness height and an additional wall-normal distance to ensure the safety of the hotwire probe. As a result, Figs. 9 and 10 may not represent a fair comparison.

To investigate how the measurement technique affects the measured energy, energies are computed at all streamwise locations using a 42% velocity cutoff. This higher cutoff increases the uncertainty in the wall location as less near-wall data is available for extrapolating to the wall location. Additionally, it systematically underestimates energy from the E_{rms} integral. This is illustrated in Fig. 11. The plot on the left shows a typical boundary layer profile downstream of the roughness. The vertical dashed line represents a 42% cutoff. As the cutoff height is applied to the U'_{rms} disturbance on the right side of Fig. 11 and subsequently extrapolated to zero at the wall location it is clear that a significant
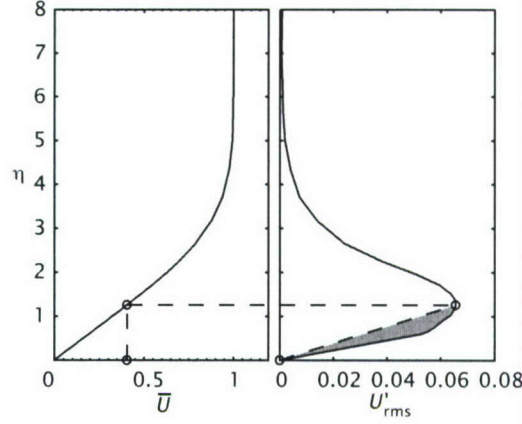
16

Figure 11: The systematic error in the U'_{rms} profile introduced by applying a velocity cutoff of $\overline{U} = 0.42$

portion of the U'_{rms} profile is neglected. As a result, E_{rms} is systematically lower for this higher cutoff; Fig. 12 verifies the lower energy estimates. However, this figure also shows that the energy jump at the trailing edge of the roughness that is observed in Figs. 9 and 10 is an artifact of the data collection approach. Using the consistent velocity cutoff (Fig. 12) it is clear that the energy grows smoothly.

The best energy estimates are those that are generated from the most complete data: Figs. 9 and 10. However, Fig. 12 gives a better indication of the energy growth trends as the disturbances move from the rough to the smooth surface. In particular, it appears as if E_{λ_k}, $E_{\lambda_k/4}$ and perhaps $E_{\lambda_k/3}$ grow quadratically over the roughness and linearly for a short distance downstream of the roughness. At the boundary between the quadratic and linear regions the energy levels and slopes match. A phenomenological argument can be made for this change in energy growth based on the work of White et al. (2005). For some disturbances measured by White et al., the energy downstream of a discrete element grew and decayed as

$$E(x) = a\,(x - x_k)\exp\left(-\frac{x - x_k}{b}\right).$$

If the disturbance is in the near field of the roughness, $x - x_k \ll b$ and $E \approx a\,(x - x_k)$. For distributed roughness, if it is assumed that the energy input per unit streamwise distance is constant then $dE = C\,dx$ where dE is the energy input across a length dx over the roughness patch. Using this concept and integrating with respect to a dummy variable ξ, the disturbance energy over the roughness ($x < x_{TE}$) would be

$$E(x) = \int_{x_{LE}}^{x} Ca\,(x - \xi)d\xi = \frac{Ca}{2}(x - x_{LE})^2$$

where the subscripts LE and TE denote the leading and trailing edges of the roughness respectively. Downstream of the roughness there is no additional energy input so the upper bound of the integral becomes x_{TE} and $x > x_{TE}$. This yields

$$E(x) = \int_{x_{LE}}^{x_{TE}} Ca\,(x - \xi)d\xi = Ca(x_{TE} - x_{LE})\,(x - x_k)$$
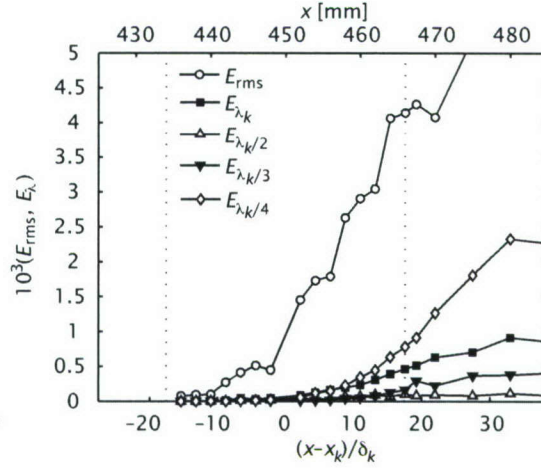
17

Figure 12: A selected portion of the disturbance energy evolution for $Re_k = 227$ using a consistent 42% velocity cutoff

because $x_k = (x_{TE} + x_{LE})/2$. As this expression shows, the disturbance energy downstream of the roughness is linear in x and proportional to the streamwise length of the roughness. Additionally, this expression shows consistent linear growth from the middle of the roughness patch. Using these relations to model the energy growth of $E_{\lambda_k/4}$ in Fig. 12 results in fairly good correlations. Notwithstanding the systematic error in E_{rms} and the assumption of constant energy input per unit streamwise distance, there appears to be a basis for the apparent quadratic-to-linear change in E_{λ_k} and $E_{\lambda_k/4}$.

The results for the $Re_k = 164$ are qualitatively similar to the $Re_k = 227$ case. For this reason, detailed U and U' distributions are not shown here, but are available elsewhere (Downs 2007). The disturbance energy evolution for the $Re_k = 164$ case is shown in Fig. 13. In this case, the total disturbance energy strictly decays from its maximum value at $x^* = 26$ to slightly more than half of that maximum value at $x^* = 206$. Periods of weak transient growth are observed in the $\lambda_k/4$ and λ_k disturbance energies. As before, the $\lambda_k/4$ disturbance energy is initially the dominant mode, reaching a peak of approximately half of the total disturbance energy by $x^* = 51$ and then decaying to about one-third of its initial value. The λ_k disturbance energy grows over a longer length, reaching its peak of about one-third of the total disturbance energy at $x^* = 155$ and becomes the dominant mode. It too begins to decay in the test region. The $\lambda_k/3$ disturbance energy undergoes slight growth, reaching an apparent plateau at $x^* = 77$. The $\lambda_k/2$ disturbance energy strictly decays. Of the three modes that exhibit transient growth, the trend observed is that longer wavelengths grow and decay over longer streamwise distances. This trend is also observed for the $Re_k = 227$ case. These two configurations invite a discussion of an Re_k^2 energy scaling as used by White et al. (2005) and the U_∞ scaling of Fransson et al. (2004); this is addressed below.

3.4 Distributed roughness results: Supercritical flow

For the $Re_k = 301$ case, selected steady disturbance profiles are shown in the bottom right corner of Fig. 14 for $x^* = 29$, 86 and 230 ($x = 475$, 525 and 650 mm respectively). When compared with the steady disturbance profiles for the $Re_k = 227$ case, two initial observations can be made. First, as U_∞ and consequently Re_k is increased, the disturbance amplitudes increase. At $x^* = 26$ the peak amplitude of the U'_{rms} disturbances increases from to 0.08 in the $Re_k = 227$ case to approximately 0.105 in the $Re_k = 301$ case (note that these plots represent slightly different dimensionless streamwise locations).
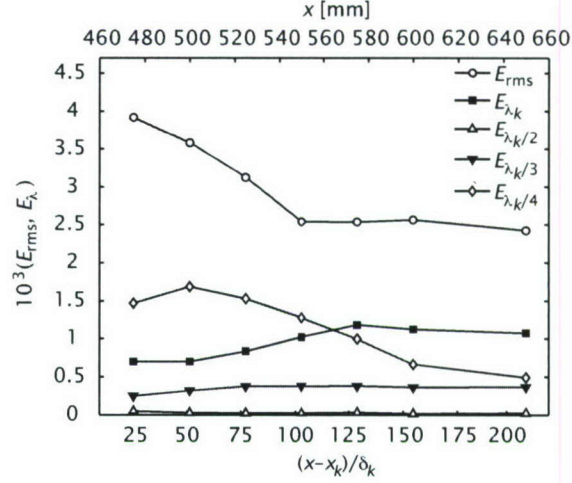
18

Figure 13: Disturbance energy evolution for $Re_k = 164$

As before as the disturbances move downstream, they move higher into the boundary layer, broaden and decrease in maximum amplitude. Second, the steady disturbance profile at $x^* = 230$ has taken on a markedly different shape from the other profiles. This is the manifestation of turbulence that is observed for this case.

Steady iso-velocity contour lines and unsteady fluctuation velocity contours are shown in Fig. 14. At $x^* = 29$ (in the top left corner of Fig. 14), the same three decelerated regions are evident as in the $Re_k = 227$ case but the magnitude and vertical range of the disturbances is greater than before. This increased level of disturbance is accompanied by an increased fluctuation intensity, particularly at around $z/\lambda_k = 0.25$. Similar trends are evident at $x^* = 86$; increasing the Reynolds number has the effect of increasing the magnitudes of both U' and u'. Because the unsteady fluctuations are locally unstable in the basic state associated with the distorted steady flow (Ergin and White 2006), this connection between higher U' and u'_{rms} is to be expected. Moving downstream to $x^* = 230$, the u' fluctuations have grown large enough in magnitude and range to saturate most of the plot. This indicates that localized turbulent bursts are beginning to contaminate the measurement domain. Also, the $\overline{U}$ profile for $x^* = 230$ is beginning to diverge from the upstream laminar basic state profiles toward a shape indicative of a turbulent boundary layer profile.

The disturbance energies for the $Re_k = 301$ case are shown in Fig. 15. The laminar region to the left of the vertical line at $x^* = 144$ is considered first. The total disturbance energy grows only marginally between the trailing edge of the roughness and its maximum value that occurs at $x^* = 57$. Thereafter, it decays until turbulent bursts begin at $x^* = 144$. As with the other two configurations, the $\lambda_k/4$ mode is the dominant spanwise disturbance mode. At the trailing edge of the roughness it represents about one-third of the total disturbance energy. It continues to grow while E_{rms} decays and at $x^* = 57$ it represents slightly more than half of the total disturbance energy. Meanwhile, the longer-wavelength modes λ_k and $\lambda_k/3$ have grown slightly and comprise most of the remaining total disturbance energy. The higher modes have all decayed to negligible amplitudes and the $\lambda_k/2$ mode remains at an essentially constant, low amplitude throughout the domain. Because of the localized breakdown to turbulence, only part of the measurement domain can be used for the study of transient growth. However, upstream of $x^* = 144$, the behavior of the disturbance energies appears to be qualitatively similar to that of the other two configurations.
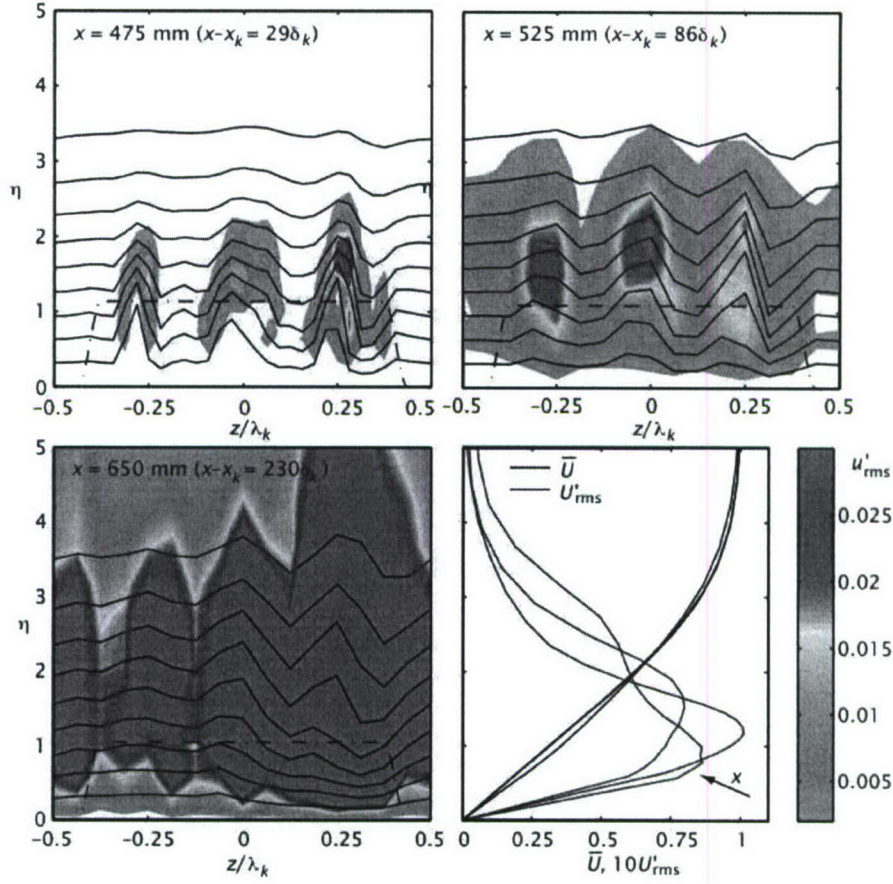
19

Figure 14: Velocity contours and fluctuation velocity field for $Re_k = 301$; basic state and steady disturbance profiles corresponding to the contour plots are shown in bottom right. Steady velocity contours are at increments of $0.1U_\infty$
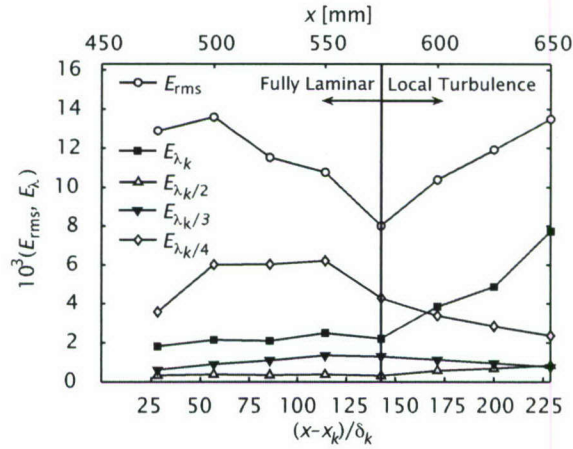

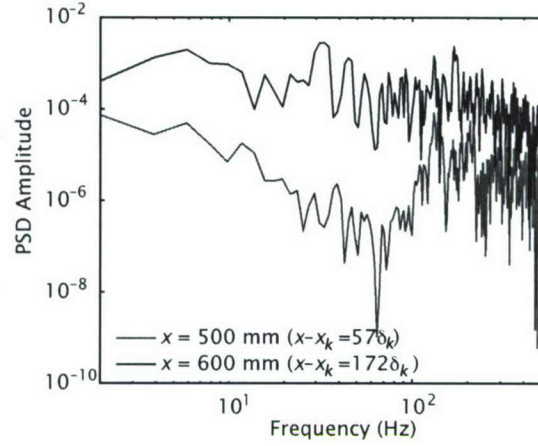Figure 15: Disturbance energy evolution for $Re_k = 301$

Figure 16: Temporal power spectral density for the $Re_k = 301$ case at $(x^*, \eta, z/\lambda_k) = (57, 1.9, 0.25)$ and $(172, 1.78, 0.25)$

Localized transition is observed to occur aft of $x^* = 144$ for the $Re_k = 301$ case. This occurs first at $z/\lambda_k = 0.25$; this spanwise location corresponds to the largest positive roughness height in the roughness field. The points neighboring $z/\lambda_k = 0.25$ remain highly disturbed, but laminar. This determination is first made using the temporal spectrum of the unsteady velocity measurements. Two such spectra are shown in Fig. 16 for $x^* = 57$ and $x^* = 172$. These points correspond to a spanwise location of $z/\lambda_k = 0.25$ and wall-normal locations of $\eta = 1.90$ and $\eta = 1.78$ respectively (these are the approximate locations of maximum u'_{rms} at this spanwise location). The $x^* = 172$ spectrum exhibits the characteristics of turbulence, while the $x^* = 57$ spectrum is of much lower magnitude. This is confirmed by the contour plots of the fluctuation velocity fields. As shown in Fig. 14, the fluctuation velocity field has saturated the color scale ($u'_{rms} = 0.03$) at $z/\lambda_k = 0.25$. As the flow moves further downstream, this local turbulence begins to contaminate neighboring areas. Had measurements been made further downstream, it is expected that the flow would become uniformly turbulent across the span, and that the spanwise variations of the U and u'_{rms} fields associated with particular roughness features would gradually disappear.

The manifestation of this local turbulence in the steady disturbance energy is shown on the right half of Fig. 15. In this section of the plot, the disturbance energy appears to undergo additional growth. This is due to the effect of the turbulence on the steady disturbance profiles; it is not due to transient growth. As shown in Fig. 14, the steady disturbance profile for $x^* = 230$ has a different shape than any of the other steady disturbance profiles. This is due to the spanwise juxtaposition of laminar and turbulent flows. By taking the spatial root-mean-square in the spanwise direction, the effect of the local turbulence is the lower lobe in the steady disturbance profile. As the disturbance energy is the integral of the square of this profile, the addition of this second lobe will markedly increase the value of this integral. Thus, the effect of the local turbulence is an apparent increase in the total disturbance energy. As the turbulence spreads across the span, turbulent mixing will surely decrease spanwise variations in U and hence, the steady disturbance energies.

To determine the nature of the transition mechanism, the streamwise evolution of the u'_{rms} profiles is considered. Ergin and White (2006) found there was significant variation in the u' levels behind each roughness element. Here, the use of the manufactured roughness produces better spanwise uniformity (see Fig. 17) so it is possible to consider spanwise phase-locked averaged u'_{rms} profiles. Such profiles
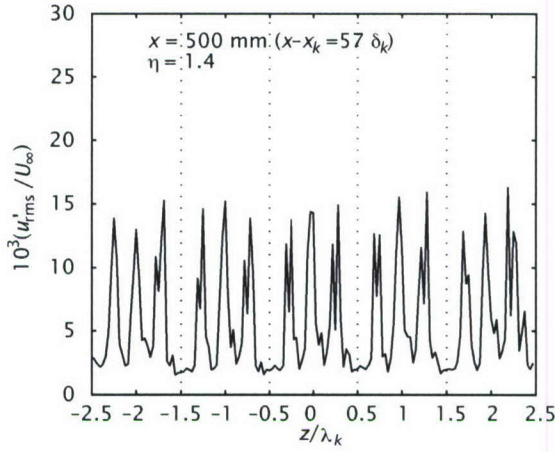
Figure 17: Fluctuation velocity line profiles for five roughness patches for $Re_k = 301$ at $x^* = 57$ mm and $\eta = 1.4$

are shown in Fig. 18 for $z/\lambda_k = 0.25$ and in Fig. 19 for $z/\lambda_k = \pm 0.5$ downstream of the roughness flats. Except for the most upstream position, a single maxima in the u'_{rms} profile downstream of the roughness is observed at approximately $\eta = 2.5$. TS waves typically have fluctuation maxima near $\eta = 1$ and 5, higher and lower than the single location observed here. Although the number and location of the maxima are not foolproof evidence of non-TS breakdown, the fact that TS-like profiles are never observed makes it unlikely. This conclusion is reinforced by the fact that there does not appear to be any unusually high signal power in the unstable TS band of the frequency spectra in Fig. 16 (the unstable TS band for these conditions is approximately 60 to 150 Hz). Rather, the transition observed here appears to be via the bypass mechanism described by Ergin and White (2006). That is, the steady disturbances produced by the roughness provide an unstable basic state in which the unsteady u' disturbances rapidly grow and bring about transition. This is path D of the transition roadmap. If the measurement domain was extended, it is possible that the two lower Reynolds number cases may have generated TS waves leading to transition. The growth and breakdown of these waves would likely be affected by the steady disturbances and would therefore represent a path B transition scenario.

The behavior observed here is quite different than that observed by Corke et al. (1986). Corke et al. performed experiments in which distributed roughness had the effect of increasing TS wave growth rates and accelerating the onset of transition, a path B transition scenario. Those experiments utilized two different strips of roughness and two freestream speeds which resulted in Re_k values that ranged from 101 to 143. The u'_{rms} profiles given by Corke et al. were used as an indication of the TS nature of the eventual breakdown. It was noted that the development of an inner maximum near $\eta = 1.72$ and an outer maximum near $\eta = 5.2$ in these profiles is a strong indication of a TS mechanism. But as noted above, the u'_{rms} profiles in the current experiment develop only a single maximum at approximately $\eta = 2.5$. Transition in the $Re_k = 301$ case is not via the same mechanism as the transition observed by Corke et al.

It has been observed that increasing Re_k of isolated roughness elements results in an increased steady disturbance magnitude (White and Ergin 2003; Fransson et al. 2004; White et al. 2005). The same phenomenon is observed here for distributed roughness. Scaling the disturbance energies for each test case using Re_k^2 as suggested by White et al. (2005) and using the x^* normalization, the
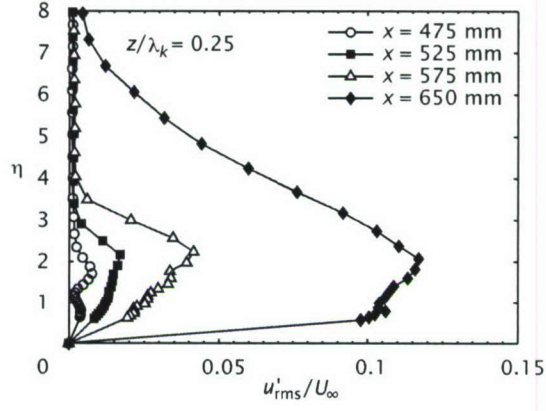
Figure 18: Phase-lock-averaged fluctuation velocity profiles for $z/\lambda_k = 0.25$, $Re_k = 301$ at selected streamwise locations ($x^* = 29$, 86, 144 and 230)
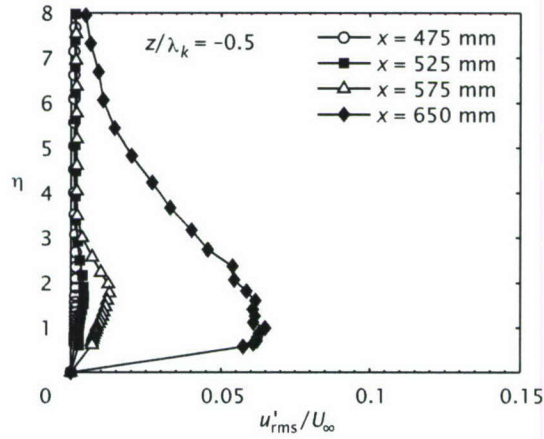

Figure 19: Phase-lock-averaged fluctuation velocity profiles for $z/\lambda_k = \pm 0.5$, $Re_k = 301$ at selected streamwise locations ($x^* = 29$, 86, 144 and 230)
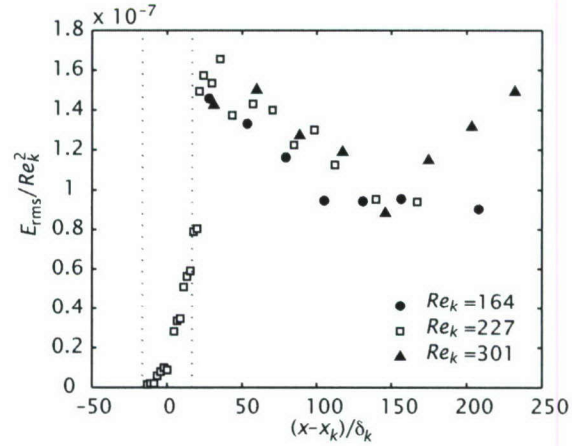
Figure 20: Scaled disturbance energy evolution for all three test cases. The vertical dashed lines indicate the streamwise location of the roughness
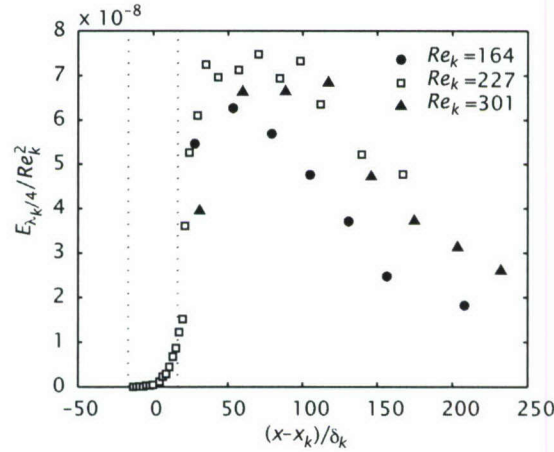
Figure 21: Scaled $\lambda_k/4$ disturbance energy evolution for all three test cases. The vertical dashed lines indicate the streamwise location of the roughness

E_{rms} data collapse to a common curve as shown in Fig. 20. It appears as if the Re_k^2 energy scaling remains appropriate for the more complicated roughness configuration considered here. A similar plot showing the normalized $E_{\lambda_k/4}$ disturbance component for the three test cases is shown in Fig. 21. The collapse of the individual mode energy is not as clean as the overall disturbance energy. This may be a consequence of the fact that $\lambda_k/4$ represents a slightly different nondimensional wavelength in each case. In the overall disturbance energy plot (Fig. 20) this variation would not be as pronounced because a wide range of wavelengths make up the total disturbance.

3.5 Conclusions

This portion of the experimental work involves measurements of steady and unsteady boundary layer disturbances that are generated by quasi-random distributed roughness. The intent is to extend earlier experimental work that used spanwise-periodic arrays of discrete cylindrical roughness elements to surfaces more similar to what is found in engineering practice. The use of spanwise-periodic arrays of

roughness patches is an intermediate step toward performing experiments using a fully rough surface. Single component hotwire anemometry is employed to make boundary layer velocity measurements above and in the wake of the distributed roughness and the measurements are phase-locked averaged in span.

What results is a finely resolved three-dimensional grid of velocity measurements downstream of a single representative patch. The steady disturbances, U', undergo transient growth for all three configurations: $U_\infty = 7.5$, 9.3 and 11.5 m/s corresponding to $Re_k = 164$, 227 and 301, respectively. Although the total disturbance energy shows little evidence of spatial disturbance growth downstream of the roughness patches, decomposing the total disturbance energy into its spanwise components yields evidence of transient growth. In particular, the $\lambda_k/4$ and λ_k spanwise disturbance modes exhibit the transient growth phenomenon. While the $\lambda_k/3$ mode did appear to undergo some transient growth, it is less significant than the two aforementioned modes. The $\lambda_k/2$ mode appears strictly to decay. This reinforces the finding that, in practice, disturbances are not optimal but rather grow or decay in a manner determined by the details of that particular disturbance's receptivity process (White 2002; White et al. 2005). Finally, as in the cylindrical roughness experiments by White et al. (2005), it is observed that these disturbances scale with Re_k^2.

Measurements above the surface of the roughness are made in the $Re_k = 227$ configuration. The simple linear growth, exponential decay model for disturbance energy evolution downstream of a cylindrical roughness element put forth by White et al. (2005) is extended to the current distributed roughness configuration. This yields a phenomenological basis for energy growth that is quadratic above the roughness and linear aft of the roughness. This argument rests on the assumption that the distributed roughness provides constant energy input per unit streamwise distance.

For the transitional configuration ($Re_k = 301$), comparison of the fluctuation velocity profiles with those of Corke et al. (1986) indicates that the observed transition for this case is not due to a TS mechanism. Instead, transition is of the type observed by Ergin and White (2006). Ergin and White found that rapid transition downstream of isolated 3D elements can be characterized as a competition between unsteady disturbance growth and stabilizing relaxation of the steady flow. This bypass mechanism is the nature of the transition that is observed in the $Re_k = 301$ configuration. Although transition is not observed for the $Re_k = 164$ and 227 cases, it is possible that the eventual transition for these cases may have been due to a TS mechanism.

Real aerodynamic surface roughness can be characterized as completely random and existing everywhere on a surface. Thus, to extend this work the next step requires making measurements above rather than in the wake of a surface which is uniformly rough. To do this, it will be necessary to develop a method of separating the effects of distributed receptivity and transient growth of the resulting flow disturbances. Once this is accomplished, it may become possible to predict the transition behavior of the boundary layer given some statistical information about the surface roughness.

4 Decomposition of Experimentally Measured Data

Single-frequency TS waves represent a discrete eigenmodes of the OSS system. At a specified frequency, spanwise wavenumber and Re_δ, a discrete eigenmode exists with a certain (complex) streamwise wavenumber α and wall-normal (complex) mode shapes for the velocity and pressure perturbations. The complex streamwise wavenumber allows for both a streamwise wavelength and exponential growth or decay in the streamwise direction; the complex mode shapes allow for phase variations in the wall-normal direction.

Transient disturbances are fundamentally different that TS disturbances. In the transient growth scenario, one specifies a frequency (which may be $\omega = 0$ to represent stationary disturbances), a spanwise wavenumber β and Re_δ and may find that no exponentially growing solutions exist; only decaying modes can be identified. Nevertheless, *algebraically* growing disturbances may still be observed. The reason is that the OSS system admits a continuous spectrum of eigensolutions in addition to the discrete solutions that are manifested as TS waves. Transient disturbances are composed of all the modes of the continuous spectrum each of which has a particular complex amplitude. Because the OSS system is not self-adjoint, the various continuous modes are not orthogonal. So, in spite of the fact that all the continuous modes decay, their non-orthogonality allows for some transient algebraic growth prior to eventual exponential decay (Schmid and Henningson 2001; Reshotko 2001). Figure 2 illustrates the algebraic-growth, exponential-decay process.

As described earlier, *optimal* transient disturbances have been identified by Andersson et al. (1999), Luchini (2000) and Tumin and Reshotko (2001) to be stationary disturbances with $\beta = 0.45$. These disturbances are initially counter-rotating streamwise-oriented vortices that induce streamwise-oriented streaks of low-speed and high-speed fluid. The optimal disturbance represents one particular collection of complex amplitudes for the continuous spectrum modes. The experiments by White (2002) and White et al. (2005) establish that roughness-induced disturbances are not optimal; roughness-induced disturbances must be represented by a collection of continuous-mode amplitudes that differs from the optimal amplitudes. However, this difference has never been quantified and no receptivity theory exists to describe how particular roughness features might affect the continuous mode amplitudes. If such a theory existed, it might be possible to predict the nature of the transient growth resulting from a particular roughness configuration. The result would be a clearer link between stability theory and experimental measurements of transient growth.

In order to link stability theory to experiment measurements, it is useful to consider how steady disturbances are decomposed. First, velocities are measured in a spanwise/wall-normal plane. Typically, just streamwise u velocities are measured but spanwise w velocities have also been measured in the experiments by Ergin and White (2005). Once these velocities have been obtained in a plane at a particular x location, time averages are computed at each location; an interpolation procedure is used to place the measurements onto a rectangular y, z grid; and spanwise phase-locked averaging is performed. Next, the basic state $\overline{U}$ profile is computed and subtracted from each z location to give give $U'(y, z)$ and $W'(y, z)$ at each x location. (The basic state $\overline{W} = 0$ so $W = W'$.) Finally, all the x locations can be combined to give a 3D stationary disturbance field

Within the context of linear stability theory, it is more useful to consider disturbances to be functions of a spanwise wavenumber β rather than z. This is accomplished in the theory using a continuous Fourier transform

$$U'(x, y, z) = \frac{1}{2\pi} \int_{-\infty}^{\infty} \widehat{U}_\beta(x, y) e^{i\beta z} d\beta$$

where U' and β are real but the $\widehat{U}_\beta(x, y)$ mode shapes are complex. The procedure for $\widehat{W}$ and W' is the same. For the experimental data, the reverse procedure is applied; $\widehat{U}_\beta(x, y)$ and $\widehat{W}_\beta(x, y)$ are computed using a discrete Fourier transform at β values determined by the roughness array wavelength and spanwise spacing of the hotwire measurements.

Each of the $\widehat{U}$ and $\widehat{W}$ mode shapes are composed of all the discrete and continuous modes of the

OSS system. In the theoretical context this superposition of modes is represented by

$$\widehat{U}_\beta(x,y) = \frac{1}{2\pi} \sum_{p,\omega} \int C_{\alpha(k),\beta}\,\phi_{\alpha(k),\beta}(y)\,e^{i\alpha(k)x}\,dk + \frac{1}{2\pi} \sum_j C_{\alpha_j,\beta}\,\phi_{\alpha_j,\beta}(y)\,e^{i\alpha_j x}.$$

In this expression, the C values are complex amplitudes, ϕ's are complex mode shapes, k is a continuous real value that parametrizes the two branches of the continuous spectrum, p and ω, j is an index representing discrete eigenmodes and $\alpha(k)$ and α_j are complex streamwise wavenumbers. Linear stability calculations give ϕ and α for each k or j. Those calculations do not give the amplitude coefficients C; those values would be predicted by a receptivity theory (if one existed) or should be measured in an experiment via a decomposition of $\widehat{U}$ data using an inverse transform of the equation given above.

Unfortunately, while the Fourier transform from z to β coordinates is straightforward using experimental data, the subsequent decomposition into C's, ϕ's and α's is not. The Fourier modes are orthogonal sines and cosine functions so an inverse Fourier transform is simple to perform. However, the ϕ modes and their associated eigenvalues α need to be calculated from linear stability theory (not a trivial task, especially for stationary disturbances) and, because these ϕ's are not an orthogonal set, a biorthogonal decomposition must be performed using the adjoint eigenmodes, $\widetilde{\phi}$ which must also be calculated numerically.

The entire procedure for the decomposition into OSS eigenmodes, ϕ, is described by Tumin (2003). Tumin finds that the required input data for such a decomposition consists of all three velocity perturbations, $\widehat{U}$, $\widehat{V}$ and $\widehat{W}$, the perturbation pressure, and the streamwise derivatives of the three velocity perturbations for a certain x plane. Because only $\widehat{U}$ can and $\widehat{W}$ can be measured with relatively low uncertainty in an experiment, certain assumptions must be made about the form of the disturbance if the decomposition is to proceed. Even then, numerical stability and other considerations make it unclear whether such a decomposition can be achieved (Tumin 2003). It is the objective of this experiment to determine whether U and W measurements made using multiple slanted hotwire probes can be used as inputs to Tumin's method of biorthogonal decomposition. If yes, it is of interest to determine whether the C amplitudes the decomposition provides are sufficiently accurate to predict the downstream evolution of the disturbance energy. If no, it is of interest to explore alternative decomposition techniques that might provide better predictive result by, perhaps, using information from more than one x location.

The measurements and analysis in support of this objective have only been partially completed. As described above, the work on the present effort at Case Western Reserve University was terminated after two of three project years and work is continuing under the auspices of a new AFOSR-funded grant at Texas A&M University. Efforts described in this report include preliminary results for multicomponent velocity measurements in the wake of a spanwise array of cylindrical roughness elements, results of a verification experiment seeking to show that the measurement approach taken before was correct and a description of ongoing efforts that may overcome obstacles to the biorthogonal decomposition approach.

4.1   Multicomponent measurements of stationary disturbances

In order to correctly capture transient growth behavior and, in particular, early details of the process that are relevant to receptivity, it is critical to measure velocity components that constitute streamwise vorticity: V' and W'. This requires the use of slanted hotwire probes capable of measuring W' as described above in Sec. 2. Therefore, first objective of the present work's attempt to decompose

experimental data into continuous-spectrum eigenmodes is to obtain U' and W' data in the wake of a spanwise array of cylindrical roughness elements. The setup is simpler than that of the distributed-roughness experiments of Sec. 3; roughness elements are applied directly to the flat plate without the need for a roughness sheet or frame. The setup is the same as is pictured in Fig. 1 with $x_k = 300$ mm ($x_{v.l.e.} = -7$ mm), a spanwise spacing of $\lambda_k = 19$ mm, a diameter $d = \lambda_k/3$ and an amplitude of $Re_k = 202$. For these measurements the unit Reynolds number is $Re' = 764 \times 10^3$ m^{-1}. High-spatial-resolution slant-probe hotwire scans are performed that include 38 spanwise steps per λ_k.

Separating the effective cooling velocity, V_e, measured by the slanted sensors into U and W requires a careful treatment of the experimental data. First and foremost, since the two slanted sensors sweep different (y, z) planes, the data from slanted sensors are shifted such that the slanted sensors spanwise locations match with those of the the middle sensor. Despite the effort to align the boundary layer sensors with respect to the flat surface, the misalignment between the sensors cannot be avoided completely. This implies that each sensor is sweeping the boundary layer at a different height from the flat surface. However, the position of each sensor with respect to the flat surface is extremely important for multicomponent data analysis. To account for any misalignment of sensors in the wall-normal direction, the wall location is estimated for each sensor at between-roughness z stations. This means that the effective cooling velocity data recorded by each sensor has a different y array, and the V_e data obtained from all three sensors must be interpolated onto a single array of heights. Once this is completed, the spanwise and streamwise velocities are resolved from the effective cooling velocity data obtained from the slanted sensors.

With the trident design used in the multicomponent experiments, U can be measured directly from the normal boundary layer sensor in the middle, as well as indirectly from the decomposition of effective cooling velocity measured by the slanted sensors. This allows the comparison of the streamwise velocity field obtained from the slanted sensors with that obtained from the middle sensor to check the quality of the data analysis. The agreement between the two sources is excellent, indicating a satisfactory data analysis. The streamwise velocity data reported in the results section of the multicomponent experiments is obtained from the middle boundary layer sensor.

With the available streamwise and spanwise velocity components, the wall-normal velocity component, V and the wall-normal velocity perturbation, V', can be obtained by using the appropriate form of the continuity equation. The first order derivatives $\partial U/\partial x$ and $\partial W/\partial z$ in this equation are approximated by central differences and V is estimated by numerically integrating $\partial V/\partial y$ using the no-penetration boundary condition at the wall: $V = 0$ at $y = 0$. Generating derivatives from experimental data is generally to be avoided as small differences between measurements points can easily be overwhelmed by measurement uncertainties at each of the points. Nevertheless, the approach taken here is seen as the most effective means of estimating V' across the boundary layer. But, doing so requires that measurements in closely spaced x planes be obtained.

The results of the multicomponent experiments include U, V, W, and Ω_x, the steady streamwise vorticity, in the domain 310 mm $< x <$ 550 mm, 0 mm $< y <$ 4.7 mm and -9.5 mm $< z <$ 9.5 mm. The grid has variable spacing in the streamwise direction with Δx as low as 2.5 mm in the near wake of the roughness array and gradually increasing to as high as $\Delta x = 50$ mm in the far wake. The phase-lock averaged steady flow properties in the roughness wake can be seen in Figs. 22–30. In these figures the flow is into the page, the abscissa is the spanwise direction and the ordinate is the wall-normal direction, both displayed in units of millimeters. The roughness element that generates the disturbance extends between -3.17 mm$< z <$3.17 mm and is 724 μm tall. The green contour lines indicate 10% increments of dimensionless streamwise velocity U, the vector field represent the dimensionless V and W, and the colored contours represent the magnitude of the streamwise vorticity.

The heavy horizontal line segment at the top right corner is equivalent to a velocity magnitude of 10% U_∞. The colored contour levels that represent Ω_x are shown on the right-hand side of each figure and have the units of inverse millimeters. The color contour levels are the same for all figures. Warmer colors (yellow, orange, red, etc.) represent a positive streamwise vorticity (into the page), indicating a clockwise fluid rotation in these figures. Conversely, the colder colors (blue, turquoise etc.) represent a negative streamwise vorticity (out from the page), indicating a counter-clockwise fluid rotation in the figures. White indicates zero streamwise vorticity.

First, the results in the near wake is presented. Immediately downstream of the roughness array, at $x = 310$ mm, the steady flow properties are shown in Fig. 22. The lines of constant streamwise velocity indicate a decelerated region in the wake of the roughness element. The deceleration is symmetric around the roughness centerline and compact in a region directly behind the roughness element, lower in the boundary layer. The locations higher in the boundary layer are not effected by the presence of roughness as much as the lower portions. Second, the crossflow vectors (V and W) are directed downward (towards the plate) along the centerline ($z = 0$). As they approach the plate, they are directed sideways in opposite directions (away from the centerline). Then they change direction again along $z \approx \pm 3.5$ mm and turn upwards away from the plate creating two streamwise vortices centered near $y = 1.0$ mm, symmetric around the roughness centerline. These vortices appear around $z \approx \pm 2.75$ mm, which is not directly along the edges of the roughness ($z = \pm 3.17$ mm), but a small distance closer to the centerline. This observation is consistent with that by Gregory and Walker (1956) whose flow-visualization results are sketched in Fig. 31. Gregory and Walker observed a horseshoe vortex that wraps around the windward side of the roughness, pinches closer to the centerline at the leeward side close behind the roughness and then diverges from the centerline leaving a pair of trailing parallel legs downstream. The rotation direction also agrees with the trailing legs of a horseshoe vortex indicated in Fig. 31. Therefore, from this point forward, this vortex pair will be called the horseshoe pair. Expected symmetries can also be seen in Fig. 22; there is little or no spanwise velocity along the centerline, or along the edges of the spanwise wavelength ($z = \pm 9.5$ mm). The vector magnitudes are less than 5% and only one pair of vortices is distinctly visible.

At $x = 320$ mm, the steady streamwise velocity contours display accelerated flow regions along both sides ($z \approx \pm 3$ mm) of the roughness, and decelerated flow regions along the centerline (Fig. 23). These findings are in good agreement with previous findings of White et al. (2005). The crossflow vector field is similar to that in Fig. 22, with increased velocity vector magnitudes and increased streamwise vorticity. It is interesting to note that a secondary pair of vortices is starting to form outside of the existing horseshoe pair. These observations are in good agreement with Gregory and Walkers (1956) results who identified up to three vortex pairs in their flow-visualization study. Additionally, the rotation directions indicated in the section cut in Fig. 31 are similar to the measured directions in Fig. 23. A careful investigation of Fig. 31 reveals that the secondary vortex pair appears at a certain downstream distance and not directly in the wake of roughness. In the results of the present work, the secondary vortex is not present at $x = 310$ mm, (Fig. 22), is barely visible at $x = 320$ mm (Fig. 23), and will become more obvious further downstream.

At $x = 330$ and 340 mm (Figs. 24 and 25) the steady U contours are similar to those in Fig. 23, with one small difference. The decelerated region in the wake along the centerline is gradually accelerating, because of the downward flow along the centerline produced by the two legs of the horseshoe vortex. The V velocity along the centerline carries the high momentum fluid from higher parts in the boundary layer to the lower parts, as explained by Landahls lift-up mechanism. This effect is more visible for the 90% U_∞ contour line in this figure and will become clearer later in this section. At $x = 330$ mm, the secondary vortex pair is completely visible, with cores at $y \approx 1.0$ mm and $z \approx \pm 3.75$ mm. The
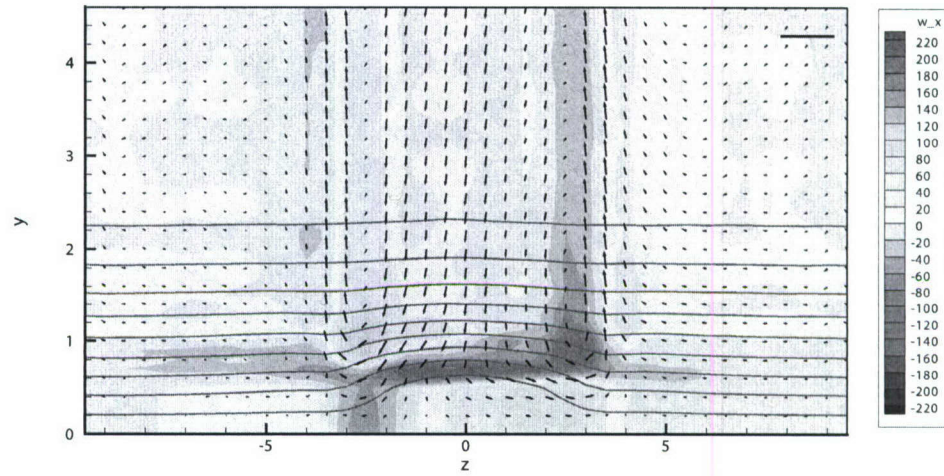
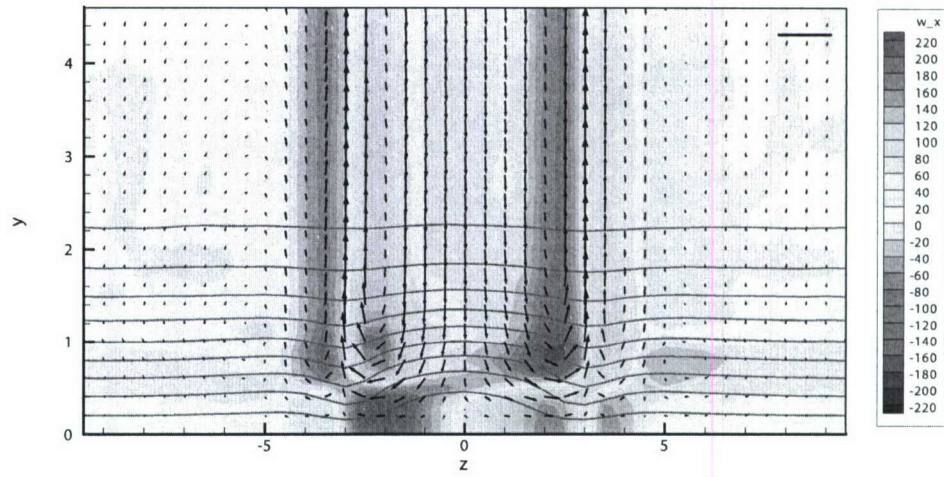Figure 22: Steady flow properties at $x = 310$ mm.

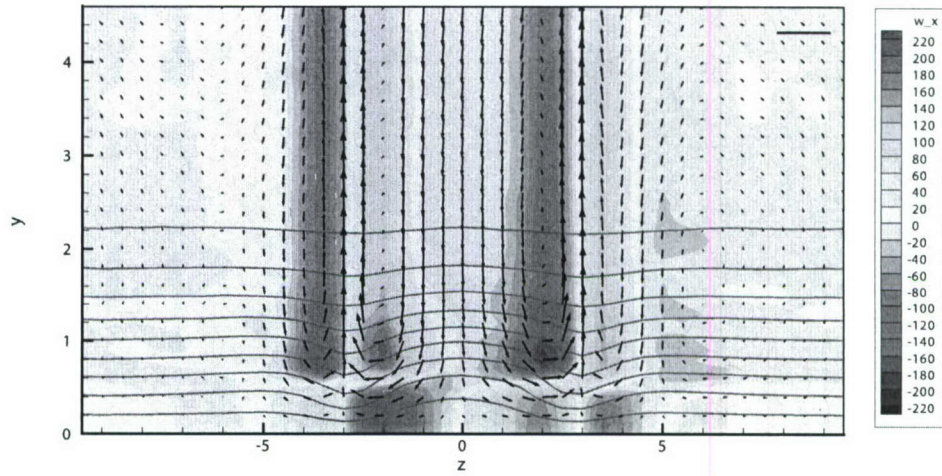Figure 23: Steady flow properties at $x = 320$ mm.

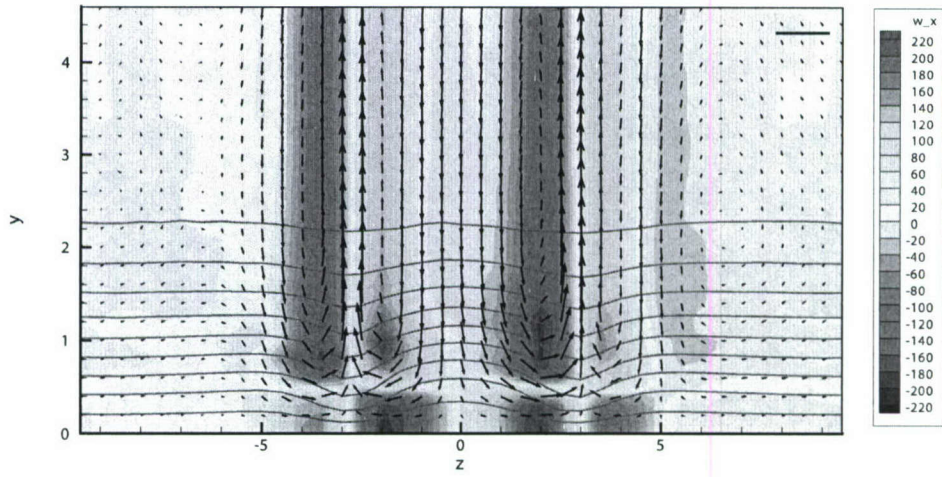Figure 24: Steady flow properties at $x = 330$ mm.

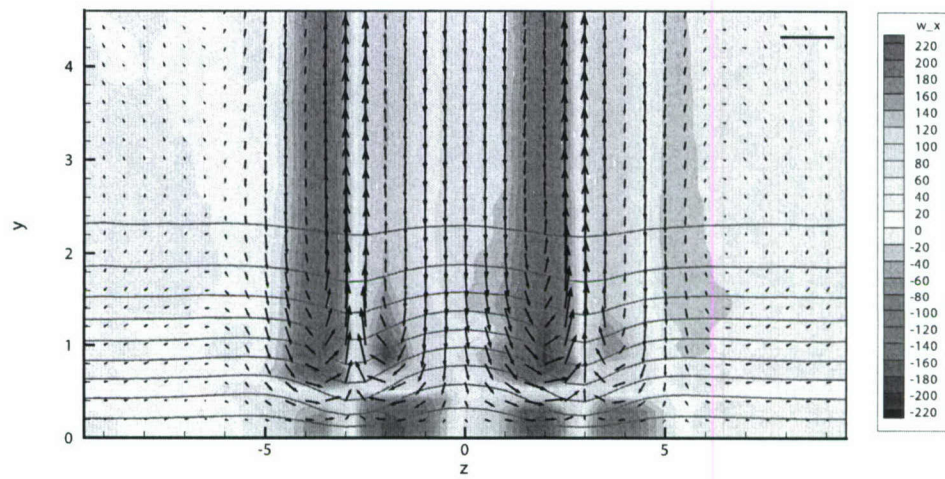Figure 25: Steady flow properties at $x = 340$ mm.

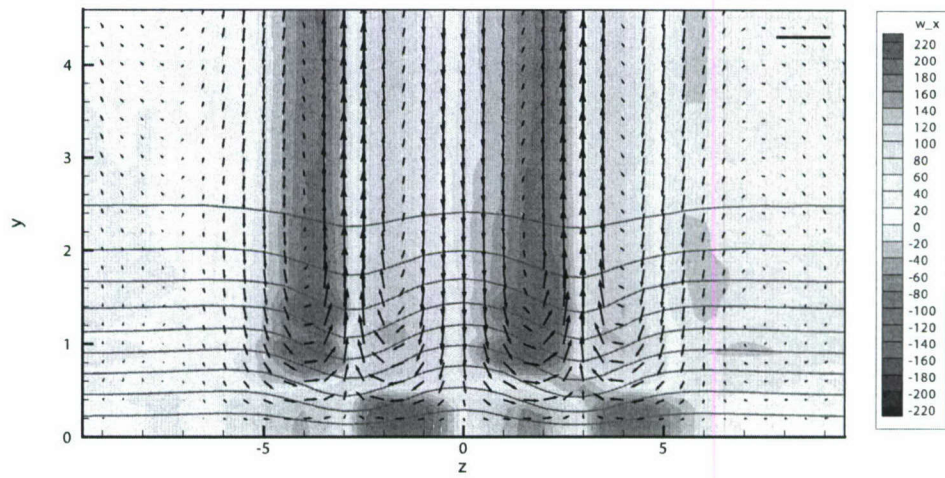Figure 26: Steady flow properties at $x = 350$ mm.

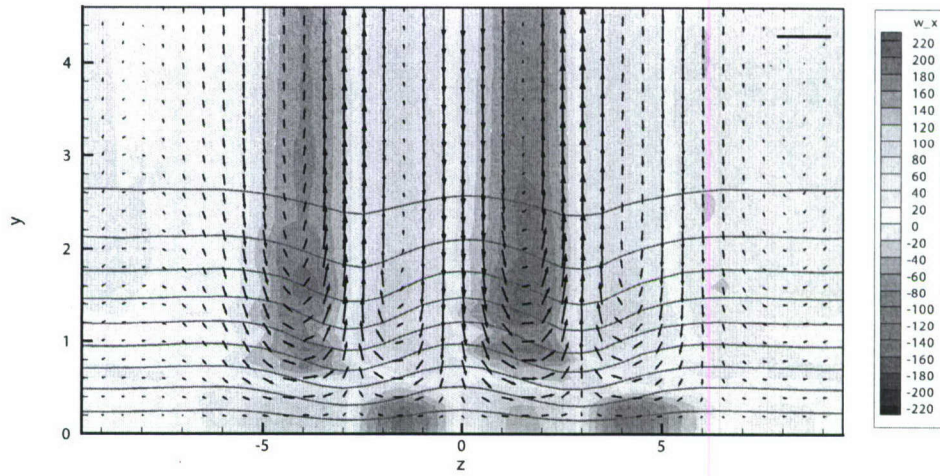Figure 27: Steady flow properties at $x = 400$ mm.

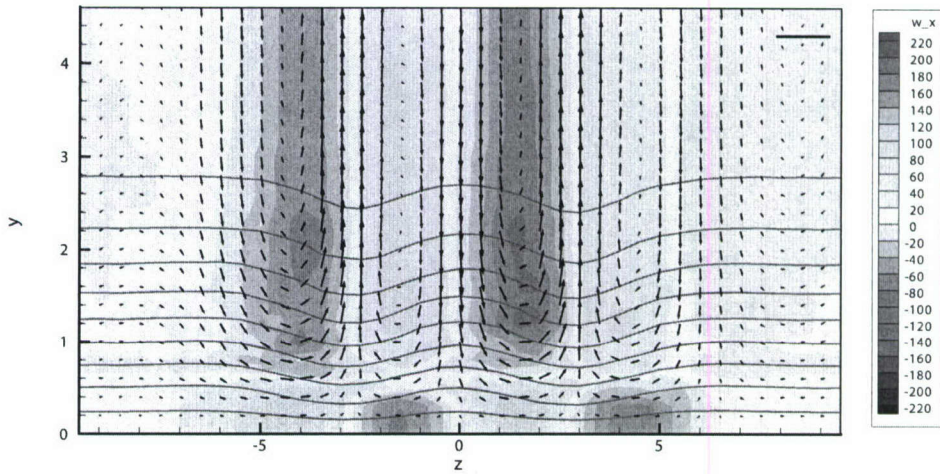Figure 28: Steady flow properties at $x = 450$ mm.

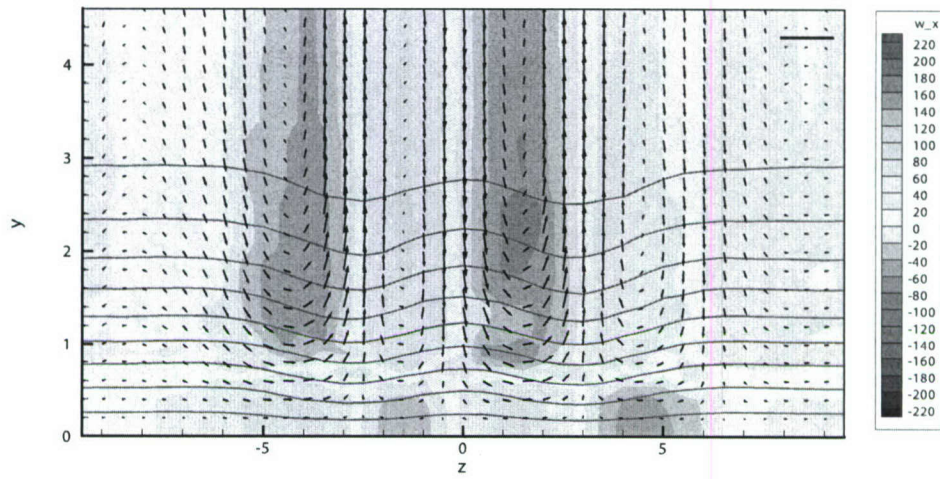Figure 29: Steady flow properties at $x = 500$ mm.

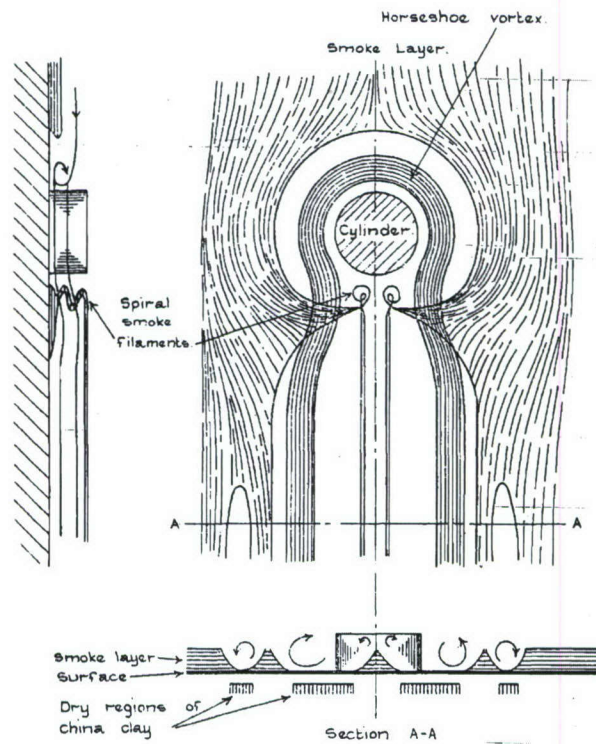Figure 30: Steady flow properties at $x = 550$ mm.

Figure 31: Flow topology in the vicinity of a roughness element (Gregory and Walker 1956).
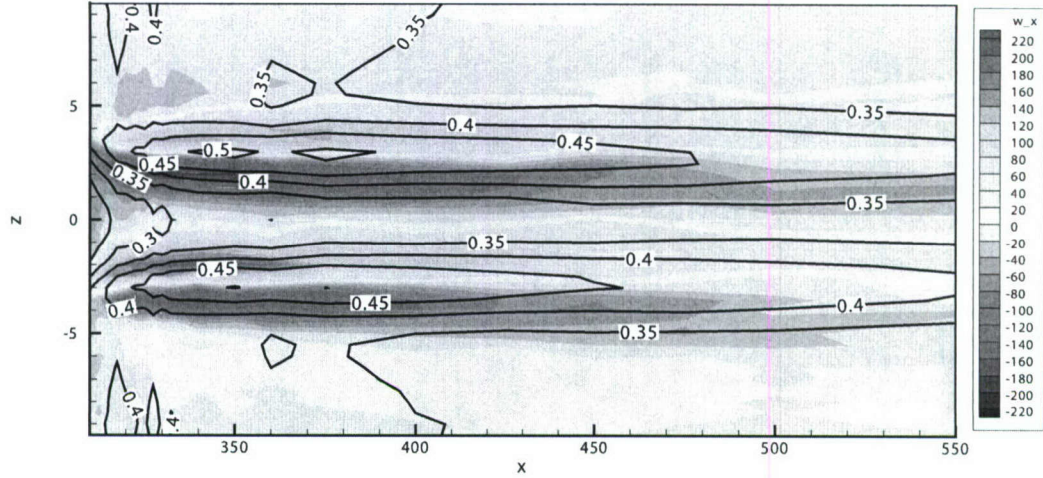
Figure 32: U and Ω_x contours 800 μm above the plate surface.

spanwise positions of the cores of the horseshoe vortices gradually approach to $z \approx \pm 2.0$ mm at $x = 340$ mm, which indicates that they have shifted closer to the centerline. More importantly, the magnitudes of crossflow velocity vectors, and therefore the Ω_x intensity are gradually increasing at $x = 330$ mm and $x = 340$ mm. The Ω_x intensity reaches its maximum value at $x = 340$ mm.

The steady flow properties in the far wake are shown in Figs. 27 through 30. In these figures, the streamwise velocity continues its gradual acceleration first in the upper parts of the boundary layer, and then in the lower parts further downstream. This is due to the downward flow along the centerline and explains the observations of Kendall (1981) on the decelerated region in the near wake and the accelerated region in the far wake. The roughness generates an initial deceleration directly behind the roughness element which is gradually reduced by the downward flow from both legs of the horseshoe vortex system. The streamwise velocity disturbance also gradually diffuses in the spanwise direction with increasing downstream distance, covering a larger spanwise region in the far wake. The crossflow velocity vector magnitudes and Ω_x intensity continue their monotonic decrease in the far wake. Additionally, four counter-rotating vortex cores at $y \approx 1.0$ mm, and their associated counterparts in the lower part of the boundary layer, all seem to cover a larger region with increasing streamwise distance.

A different perspective on the flow's development downstream of the roughness element is provided by Fig. 32 that shows the (x, z) plane 800 μm above the plate surface. This plot illustrates the process by which the decelerated region in the near-wake of the roughness element gradually evolves into a slightly accelerated flow with strongly accelerated zones (i.e., high-speed streaks) on either side of the roughness element's centerline. As initially noted by Kendall (1981), the streaks are extremely persistent with strong disturbances present 100s of millimeters downstream of the sub-millimeter-height roughness element. The symmetry about the roughness element centerline, $z = 0$, is a good indication of data quality.

A few important final points can be made regarding the wall-normal extent of the velocity per-turbations and Ω_x. At all the x locations picture in Figs. 22 through 30, V' and Ω_x both reach the edge of the boundary layer with non-zero magnitude and remain constant outside the boundary layer.

35

However, the directly measured quantities U' and W' are zero outside the boundary layer, as expected. V' and Ω_x should also approach zero outside the boundary layer and this raises concern about either the data analysis approach or the wall-normal extent of the measurements. Although the data has passed all of the other internal consistency tests (e.g., symmetry and U calculated from the slant-wire pair matching U measured by the center straight wire), the V's generated by integrating the continuity equation does not go to zero in the freestream when $V = 0$ at the wall. The continuity equation is first-order in y so only one boundary condition can be applied so $V' = 0$ can only be strictly enforced at the wall or in the freestream. Applying $V' = 0$ in the freestream and integrating toward the wall is possible but this leads to an even less appealing outcome, violating the no-penetration boundary condition at the wall.

The most likely reason for this behavior is inherent uncertainty of the velocity derivatives. Integrating in the y direction may accumulate derivative errors due to truncation, measurement uncertainty or both. Accumulation of these likely results in the failure to achieve a reasonable freestream behavior for V. Work is ongoing to resolve this problem as part of the follow-on grant at TAMU. It is important that this issue be addressed if continuous-mode decomposition is to be achieved. If V' is non-zero outside the boundary layer, the continuous-spectrum modes will take on very different amplitudes than their correct values. These modes consist of oscillatory amplitudes of constant vertical wavelength and phase outside the boundary layer. So, integrating their adjoints against a constant (but erroneous) V' in that region could overwhelm the effect of the correct behavior in the boundary layer.

4.2 Roughness-height verification experiments

It is clear that the accuracy of the experimental data is critical to making an accurate decomposition into continuous-spectrum modes. So, data from the previous AFOSR-funded effort (FA9620-02-1-0058; reported by Ergin and White 2006) was shared with a group at AFRL who performed a DNS of the same experimental setup (Rizzetta and Visbal 2007). Insofar as continuous-mode decomposition is concerned, DNS provides full knowledge of the entire disturbance field and can provide all the needed data for the decomposition. The objective is to *not* use DNS data but to use experimental data for the decomposition. Nevertheless, a successful comparison with DNS data is deemed important for verifying that the experimental data is of sufficiently good quality to proceed.

While a comparison between experimental and DNS data is never expected to be perfect, surprising differences exist between the data collected by Ergin and White (2006) (EW) and the simulation results reported by Rizzetta and Visbal (2007) (RV). Both studies used the configuration of Sec. 4.1 except used roughness heights of $Re_k = 202$ and 334. At $Re_k = 334$, RV found complete transition and fully turbulent flow about 100 mm or 158 δ_k downstream of the roughness elements (δ_k is the boundary-layer scale at the roughness location, $\delta_k = [(x_k - x_{v.l.e.})/Re']^{1/2}$) while EW reported complete transition about 240 mm or 378 δ_k downstream of the roughness elements. Additional comparisons reveal qualitative differences between the velocity contours measured in the experiments and produced by the numerical simulation.

These discrepancies prompted a reexamination of the EW experiments in comparison to previous roughness induced transition studies. As noted in Sec. 1, White et al. (2005) found that stationary disturbance energy generated by roughness elements scales as Re_k^2. While the EW results confirm this trend, the EW E_{rms}/Re_k^2 curves fall below those of White et al. (2005), White and Ergin (2003) and Rice (2004). Combined with the inconsistencies in the velocity profiles and transition location raised by the DNS, this creates concern that the EW experiments might have been flawed. Both the lower values of disturbance energy relative to the earlier experiments and the discrepancy between the

	EW, Reported		Current, Target		Current, Realized	
Parameter	low k	high k	low k	high k	low k	high k
x_k [mm]	300		412.5		412.5	
λ_k [mm]	19.00		22.84		22.84	
D [mm]	6.35		7.61		7.61	
k [μm]	714	918	862	1115	862 ± 25	1115 ± 25
$Re' \cdot 10^{-3}$ [m^{-1}]	764		632		625 ± 13	644 ± 13
δ_k [μm]	634		766		764 ± 2	810 ± 2
Re_{δ_k}	484		484		478 ± 10	520 ± 11
Re_k	202	334	202	334	202 ± 13	329 ± 21

Table 4: Experimental configuration. Parameters given in only the low-k columns apply to both the low- and high-k configurations.

experiment and the DNS point to the possibility that the values of Re_k reported in EW might have been erroneously large. The procedure used by EW — systematically increasing the roughness height between experiments at different Re_k's — means that if the reported Re_k values are incorrect, they are all in error by an amount corresponding to a constant roughness-height offset. Given the sensitivity of the decomposition procedure and the need for well-understood experimental conditions, this need motivates a repeat of the earlier Ergin and White (2006) experiment to determine whether Re_k was reported correctly.

So, it is of interest to reproduce two of the EW cases in an attempt to reconcile the discrepancies between EW and RV. To achieve this, the reported nondimensional parameters of the EW and RV studies are reproduced and the boundary layer disturbance profiles, the disturbance energy and the transition behavior are measured. To reconcile the difference in transition location between EW and RV, an $Re_k = 334$ configuration is examined. In addition, an $Re_k = 202$ configuration is also examined to ensure that previous laminar results are reproducible and that the expected Re_k^2 scaling applies.

While duplicating the experimental setup of Ergin and White (2006) might have been straightforward, in the time between the EW experiments and the present work, the plate was modified to include the roughness sheet and frame used for the distribute roughness experiments described in Sec. 3. These changes made exact duplication of the EW experiments impossible. However, it is possible to duplicate the important nondimensional parameters and that is the approach taken here. The present experiments seek to match the EW Re_k and Re_{δ_k} values while holding all length ratios equal to the EW values.

A trial-and-error approach was used to find a set of target operating conditions that would achieve the desired experimental parameters. A summary of the dimensional and nondimensional EW parameters and the target parameters of the current work is given in Table 4. These parameters give the necessary specifications to manufacture a roughness insert to be placed on the flat plate. The dimensions of the flat plate allow nine cylindrical elements arrayed at a constant streamwise location. Spanwise phase-locked averaging is performed over the center seven elements. The insert is aluminum plate with machined brass plugs serving as the roughness elements.

Because the process of attaching the roughness sheet to the flat plate requires the entire plate

be removed from the wind tunnel, it is necessary to verify alignment for zero pressure gradient with the roughness installed. Unfortunately, δ_k cannot be measured at x_k because of the presence of the elements. Nor can previous no-roughness scans be used for this purpose because installing the roughness sheet can change the pressure gradient and stagnation point location. Alignment was verified using a series of boundary layer scans performed in the region just upstream of the roughness elements and far downstream of the roughness in the fully laminar configuration. Wall-normal velocity profiles are used to calculate boundary layer integral quantities, δ^* and θ, upstream of the roughness and fits to these curves are used to determine the boundary layer thickness scale, δ_k. The results of this process, the realized experimental parameters, are given in Table 1. These show some small discrepancies with the target values. However, the match is quite good for the term of primary interest, Re_k. Given the complexities of properly repeating a previous experiment, the setup is judged to be adequately close to that used by EW to proceed.

Because the objective is to resolve discrepancies between numerical results of Rizzetta and Visbal (2007) and experimental results of Ergin and White (2006), specific items of interest are the transition location for $Re_k = 329$ (the Re_k value realized during the present bypass experiment), as well as velocity contours and the disturbance energy evolution. RV show a transition location somewhat upstream relative to the EW experiments and also show finer-scale structures than do EW. The present work seeks to identify these fine-scaled structures. Additionally, the present data is intended to reconcile the difference in the scaled disturbance energy, $E_{rms}/Re_k{}^2$, between EW and White et al. (2005), White and Ergin (2003) and Rice (2004).

To begin, Fig. 33 shows the evolution of the steady and fluctuating streamwise flow in the wake of the $Re_k = 329$ roughness elements. Figure 33(a) shows a distinctive jagged pattern of multiple high-and low-speed regions in the roughness wake. Within this field, the highest velocity fluctuations are focused in the area of strongest shear. As the flow progresses downstream, Figs. 33(c) and 33(d) show how quickly localized breakdown leads to turbulent wedges behind each element. Localized turbulence is evident about 59 δ_k downstream of the roughness. In the EW experiment, localized turbulent breakdown occurred starting about 79 δ_k downstream of the roughness while in the RV simulations this occurred about 65 δ_k downstream. Thus, the present experiments tend to confirm the earlier breakdown observed by RV. However, many experiments have shown the breakdown point to be quite sensitive to numerous factors (see Klebanoff et al. 1992, for example) so a large variance between similar setups is not unexpected.

Comparing these results to the EW data, the uniformity of the breakdown pattern here is striking. The fact that all of the roughness elements lead to breakdown at nearly the same x location and proceed toward fully turbulent flow at the same rate is quite different than was observed earlier. The difference might be a result of using machined roughness elements here as opposed to the paper elements used by EW.

Figure 34 compares conditions about 15 δ_k downstream of the roughness for the high-roughness configuration of EW and the present experiment. At this location, both experiments reveal jagged velocity contours that include strongly decelerated wakes behind the roughness elements. The roughness of the current experiment generates a somewhat stronger U'_{rms} profile with significantly stronger spanwise shear, $\partial U/\partial z$, than was observed by EW. Perhaps as a consequence, stronger unsteady fluctuations are measured in the current experiment than previously.

The fact that the two experiments show slightly different U'_{rms} profiles is not surprising given the sensitivity to Re_k and the difficulty in realizing a precise Re_k value. More surprising is that the two experiments' contour plots have notably different qualitative features. In particular, the current
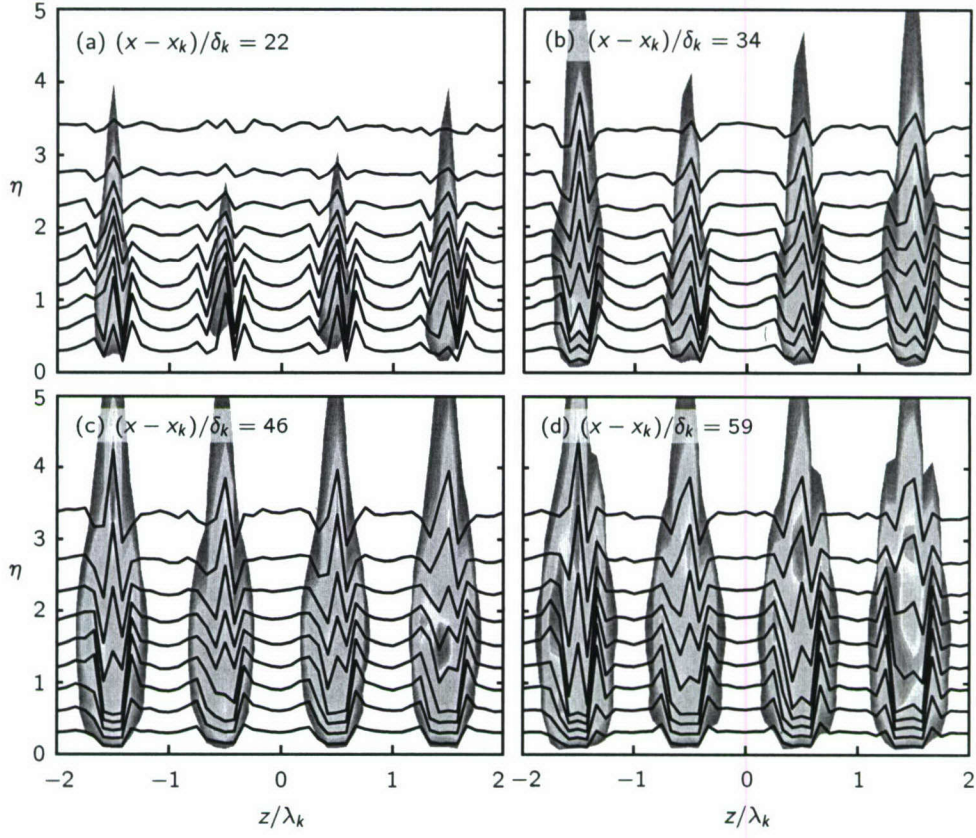
Figure 33: Steady and unsteady streamwise velocity contours for $Re_k = 329$. Black lines correspond to 10% steady-velocity contours; colors represent are u'_{rms} with a maximum value of 16% of U_∞.
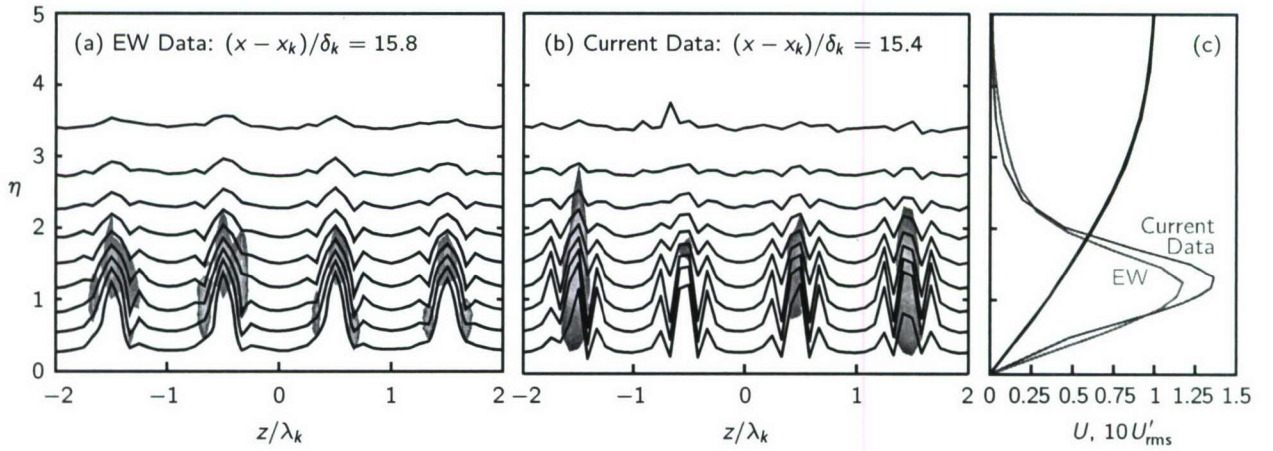

Figure 34: Near-wake steady and unsteady streamwise velocity contours and profiles. Color contour levels represent u'_{rms}; both color scales match the scale of Fig. 33
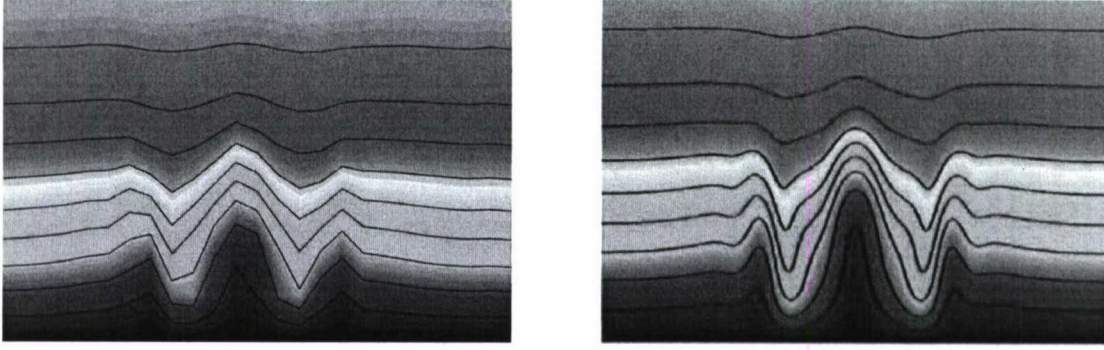
Figure 35: Near-wake streamwise velocity contours. Current experimental results for $Re_k = 329$, 25 δ_k downstream of the roughness are at left; RV simulation results for $Re_k = 334$, 32 δ_k downstream are at right.

experiments show three distinct decelerated zones whereas the EW results only show a single, broad decelerated zone behind each roughness element. The current results are more similar to the simulation results of RV than are the EW results. The reason for the different experimental results is unknown. The wider spanwise spacing (relative to the hotwire size) between the roughness elements here as compared to EW might help resolve these fine-scale features. Or, it might be that the machined, sharp-edge roughness elements used here actually produce these fine-scale features and that these were simply not present in the EW experiment that used stacked paper disks as roughness elements.

Due to the difference in transition location between EW and RV, a velocity contour comparison is not given by RV. Generally speaking, the RV contours show finer-scale features than EW and, in particular, tend to show three decelerated zones rather than EW's single zone. A comparison between RV and the present results is given in Fig. 35. (This figure uses the RV color contour spectrum that progresses from black for low speeds to magenta for high speeds. The unsteady u'_{rms} is not shown.) Both the contour shapes and disturbance amplitudes are in reasonably good agreement. The DNS satisfactorily reproduces the roughness wake, and as discussed above, the current experiments are able to capture the three decelerated zones predicted by the DNS while EW does not.

In light of the discussion to this point, the notion that the Re_k values reported by EW are incorrect remains plausible. Preliminary disturbance energy comparisons strengthened this possibility. As explained above, White et al. (2005) established Re_k^2 as a correct disturbance-energy scaling. The three EW configurations, $Re_k = 202$, 264, and 334, follow this trend but the collapsed E_{rms}/Re_k^2 curve representing the EW data is markedly different than earlier experiments (White et al. 2005; White and Ergin 2003; Rice 2004). Specifically, Fig. 36 shows that the scaled EW disturbance energy (solid square symbols) decreases more rapidly in the near wake of the roughness array and reaches a minimum value about half that of the earlier studies (solid circles). These differences could be an indication that EW's reported Re_k values are systematically too high. However, in the far-wake region, the EW energy levels grow rapidly and reach levels equal to the earlier values. Thus, the discrepancy between the experiments cannot be explained by a simple scaling error.

The current experiment's E_{rms}/Re_k^2 values, the open symbols in Fig. 36, clearly show that the scaled EW energy data is correct; no systematic Re_k error is evident. The present and earlier data are remarkably consistent considering the sensitivity of these experiments and that the current data is obtained using a wholly different set of dimensional parameters than the EW experiments. The data for $Re_k = 202$, which is most similar to EW in terms of Re_k, Re_{δ_k} and λ_k/δ_k shows an energy
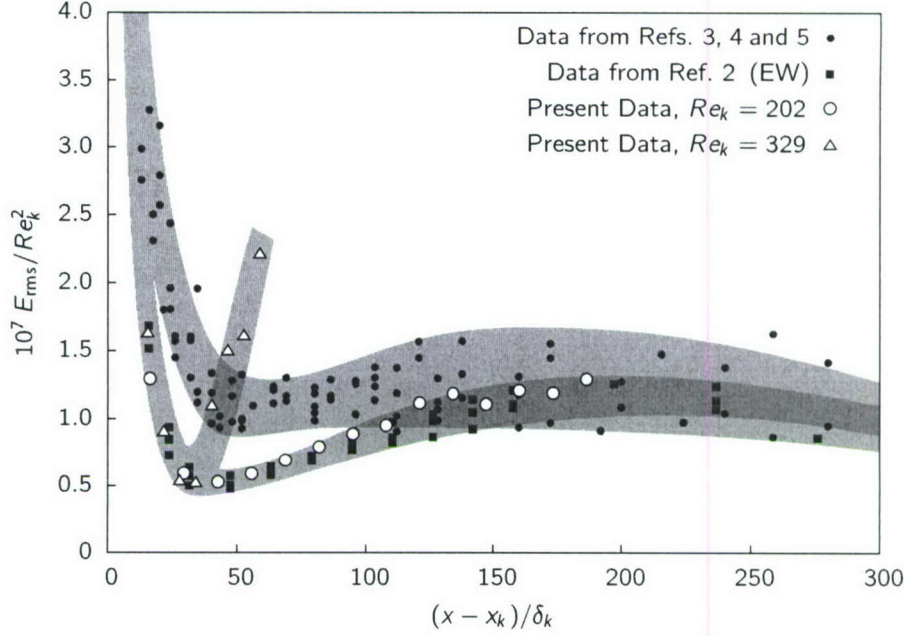
Figure 36: Scaled disturbance energies.

evolution that is completely consistent with the EW results. Furthermore, despite the more-rapid transition onset, the data for $Re_k = 329$ collapse to the EW results through the energy minimum. After that point, breakdown to turbulence begins and the energy begins to rapidly diverge as turbulence fills the boundary layer. This is only a short-lived artifact of breakdown. Further downstream, the spanwise mixing provided by turbulence would quickly act to decrease the spanwise variations in the streamwise velocity that make up the stationary disturbance energy.

In addition to validating the Re_k's quoted by EW, Fig. 36 shows an as-yet-undocumented dependence of the disturbance energy on Re_{δ_k} and/or λ_k/δ_k. The previous experiments represented in Fig. 36 were performed at somewhat lower values of Re_{δ_k} and higher values of λ_k/δ_k than the EW and current experiments. White et al. (2005) had $Re_{\delta_k} = 431$ and $\lambda_k/\delta_k = 32.8$ while EW had $Re_{\delta_k} = 484$ and $\lambda_k/\delta_k = 30.0$. This may be responsible for the differences in the E_{rms}/Re_k^2 slopes and minima. This result was unexpected and, in planning the present experiments, Re_{δ_k} and λ_k/δ_k were considered to be of secondary importance to Re_k. In fact, it appears that differences in these values may well be the source of the discrepancy between the EW and prior experimental results.

At the outset of the comparison between the EW and RV data, it appeared that EW might have incorrectly reported Re_k values as that would explain many features of the discrepancies. However, the disturbance energies obtained here reproduce the scaled values from EW provide clear evidence that the EW experiments quoted correct Re_k values. While the present experiments verify the EW energy values, velocity contours obtained in the present experiment are much more similar to the RV simulation than to the earlier EW measurements. This may be a consequence of a somewhat wider spacing between roughness elements relative to the hotwire size. Or, it could be that the sharp-edged roughness elements used here are more similar to the precise computational boundaries imposed by RV and these sharp edges are actually responsible for the fine-scale features of the velocity contours.

If the discrepancy is because the EW measurements did not fully resolve the spanwise variations

of U, it is possible that this may be the source of the non-zero V' values in the freestream discussed at the end of Sec. 4.1. Failure to properly resolve $\partial W/\partial z$ could result in a systematic error on $\partial V/\partial y$ that would lead to the observed behavior. This possibility is being examined further.

One important new conclusion that can be drawn from the present work is the sensitivity of the disturbance energy to Re_{δ_k} and/or λ_k/δ_k. It is thought that the discrepancy between the previous results (White et al. 2005; White and Ergin 2003; Rice 2004) and the more recent results by EW and those presented here is mostly a function of differences in these values. In the context of transient growth theory, both of these values are significant. First, λ_k/δ_k and harmonics of this nondimensional wavelength are not constant when δ_k changes but λ_k does not. Thus, EW have different nondimensional spanwise wavelengths than the earlier experiments. Therefore, each have disturbances that are made up of different distributions of continuous spectrum modes that lead to different degrees of suboptimal disturbance growth. Second, even when λ_k/δ_k is matched between experiments, if Re_{δ_k} is different, then the precise details that describe the continuous spectrum modes are different and this could result in different transient growth and decay rates. It is unclear whether the differences here can be more attributed to different nondimensional wavelengths or different Reynolds numbers. Nevertheless, the role of these factors cannot be overlooked.

4.3 Conclusion and Outlook

The decomposition of experimentally measured roughness-induced disturbances into continuous-spectrum modes remains a work in progress. Measurements made under the current grant are promising. But, more needs to be done in regards to their analysis before the decomposition outlined by Tumin (2003) can be performed. Most notably, the reason for the non-zero V' velocities in the freestream must be determined and a method must be developed that allows for more accurate reconstructions of all three velocity perturbations. This work is ongoing at TAMU.

One promising means of reconstructing the whole velocity-perturbation field is to abandon direct integration of the continuity equation in favor of a least-squares approach that would only approximately satisfy continuity but would allow for better control over boundary conditions. A similar approach has been used successfully elsewhere by Schmucker and White (2007). A rationale for this is that the integration for the V' velocity may accumulate error as it proceeds. Acknowledging that there is measurement error suggests that it may not be wise to integrate in this fashion. Instead, a least-squares approach could assess a trial (U', V', W') field based upon how closely that field matches the measured U' and W' data, satisfies continuity and other constraints. Then, the disturbance field could be iteratively improved. A Monte Carlo technique is being explored as a means of performing this iterative improvement. Once a minimum value of the error metric was found, the resulting disturbance field might provide a better input to the biorthogonal decomposition approach. Additional benefits of this approach are that the disturbance field would be smooth and continuous (unlike the measured data) and an arbitrary number of constant-x planes could be incorporated in generating the input data.

References

Andersson, P., M. Berggren, and D. S. Henningson (1999). Optimal disturbances and bypass transition in boundary layers. *Phys. Fluids 11*(1), 134–150.

Bruun, H. H. (1995). *Hot-Wire Anemometry Principles and Signal Analysis*. Oxford University Press.

Butler, K. and B. Farrell (1992). Three-dimensional optimal perturbations in viscous shear flow. *Phys. Fluids A 4*(8), 1637–1650.

Corke, T. C., A. Bar-Sever, and M. V. Morkovin (1986). Experiments on transition enhancement by distributed roughness. *Phys. Fluids 29*(10), 3199–3213.

Downs, III, R. S. (2007). Receptivity and transient growth of disturbances generated by random surface roughness. Master's thesis, Case Western Reserve University.

Ergin, F. G. and E. B. White (2005). Multicomponent and unsteady velocity measurements of transient disturbances. AIAA Paper 2005-0527.

Ergin, F. G. and E. B. White (2006). Unsteady and transitional flows behind roughness elements. *AIAA J. 44*(11), 2504–2514.

Farrell, B. F. (1988). Optimal excitation of perturbations in viscous shear flow. *Phys. Fluids 31*, 2093.

Fransson, J. H. M., L. Brandt, A. Talamelli, and C. Cossu (2004). Experimental and theoretical investigation of the non-modal growth of steady streaks in a flat plate boundary layer. *Phys. Fluids 16*(10), 3627–3638.

Gregory, N. and W. S. Walker (1956). The effect on transition of isolated surface excrescences in the boundary layer. Technical Report R. & M. 2779, Aero. Res. Council.

Hinze, J. O. (1959). *Turbulence. An introduction to its mechanism and theory*. New York: McGraw-Hill.

Jørgensen, F. E. (1971). Directional sensitivity of wire and fibre-film probes. *DISA Info. 11*, 31–37.

Kendall, J. (1981). Laminar boundary layer velocity distortion by surface roughness: Effect upon stability. AIAA Paper 81-0195.

Klebanoff, P., W. Cleveland, and K. Tidstrom (1992). On the evolution of a turbulent boundary layer induced by a three-dimensional roughness element. *J. Fluid Mech. 237*, 101–187.

Luchini, P. (2000). Reynolds-number-independent instability of the boundary layer over a flat surface: Optimal perturbations. *J. Fluid Mech. 404*, 289–309.

Press, W., S. Teukolsky, W. Vetterling, and B. Flannery (2001). *Numerical Recipes in C* (2nd ed.). Cambridge University Press.

Reshotko, E. (2001). Transient growth—A factor in bypass transition. *Phys. Fluids 13*(5), 1067–1075.

Reshotko, E. and L. Leventhal (1981). Preliminary experimental study of disturbances in a laminar boundary layer due to distributed roughness. AIAA Paper 81-1224.

Reshotko, E., W. S. Saric, and H. M. Nagib (1997). Flow quality issues for large wind tunnels. AIAA Paper 97-0225.

Rice, J. M. (2004). Roughness receptivity and scaling of non-optimal transient disturbances. Master's thesis, Case Western Reserve University.

Rizzetta, D. P. and M. R. Visbal (2007). Direct numerical simulations of flow past an array of distributed roughness elements. *AIAA J. 45*(8), 1967–1976.

Saric, W. (2007). Boundary-layer stability and transition. In C. Tropea, A. L. Yarin, and J. F. Foss (Eds.), *Springer Handbook of Experimental Fluids Mechanics*, pp. 886–896. Berlin: Springer.

Schmid, P. J. and D. S. Henningson (2001). *Stability and transition in shear flows*. New York: Springer.

Schmucker, J. A. and E. White (2007). Technique for measurement of droplet profiles for use in icing physics studies. SAE Paper 2007-01-3293.

Tani, I., A. Komoda, Y. Komatsu, and M. Iuchi (1962). Boundary layer transition by isolated roughness. Technical Report 375, Aero. Res. Inst., Tokyo Univ.

Tumin, A. (2003). Multimode decomposition of spatially growing perturbations in a two-dimensional boundary layer. *Phys. Fluids 15*(9), 2525–2540.

Tumin, A. and E. Reshotko (2001). Spatial theory of optimal disturbances in boundary layers. *Phys. Fluids 13*(7), 2097–2104.

White, E. B. (2002). Transient growth of stationary disturbances in a flat plate boundary layer. *Phys. Fluids 14*(12), 4429–4439.

White, E. B. and F. G. Ergin (2003). Receptivity and transient growth of roughness-induced disturbances. AIAA Paper 2003-4243.

White, E. B. and F. G. Ergin (2004). Using laminar-flow velocity profiles to locate the wall behind roughness elements. *Exp. Fluids 36*(2), 805–812.

White, E. B. and E. Reshotko (2002). Roughness-induced transient growth in a flat-plate boundary layer. AIAA Paper 2002-0138.

White, E. B., J. M. Rice, and F. G. Ergin (2005). Receptivity of stationary transient disturbances to surface roughness. *Phys. Fluids 17*(6), 064109.